International Journal of Mechanical Sciences 283 (2024) 109623

Contents lists available at ScienceDirect

International Journal of Mechanical Sciences

journal homepage: www.elsevier.com/locate/ijmecsci

Travelling waves in beam-like structures submerged in water

Skriptyan N.H. Syuhri [a,b,*], Hossein Zare-Behtash [a,c], Andrea Cammarano [a,c]

[a] James Watt School of Engineering, University of Glasgow, United Kingdom
[b] Department of Mechanical Engineering, University of Jember, Indonesia
[c] Department of Aeronautics and Astronautics, University of Southampton, United Kingdom

ARTICLE INFO

Keywords:
Beam structures
Submerged structures
Fluid-structure interaction
Travelling waves
Euler-Bernoulli beam
Wave-Propelled devices

ABSTRACT

There are many examples in nature of travelling waves used for propulsion purposes, e.g., micro-organisms and sea creatures. Structural travelling waves can be used to induce momentum in a surrounding media creating a net propelling force. Recent research has tried to capture this interaction in engineering devices. Nonetheless, some challenges remain to fully exploit this phenomenon so that travelling-waves propelled devices can be optimally designed. One such challenge is that the interaction between the structure and the surrounding fluid heavily influences the amplitude of the waves and how they travel through the structure. This paper proposes a systematic qualitative and quantitative analysis of travelling waves in a slender cantilever beam submerged in water. The novelty of this work is demonstrated through two key aspects: The application of the Euler-Bernoulli beam equation combined with the Galerkin approximation, enabling a deeper understanding of how travelling waves form at resonant frequencies rather than non-resonant ones; and An analytical approach using a Galerkin approximation to characterise the nonlinear fluid-structure interaction, followed by linearisation for a comprehensive parametric study of the problem. In this investigation, the contributions of the first five vibration modes are considered in relation to the travelling waves observed near the resonant peaks. Experimental tests validate the analytical results and assess the accuracy of the proposed models. The results demonstrate that the model presented effectively characterises the travelling waves, making a suitable tool for the design of travelling-wave propelled devices.

1. Introduction

Several design solutions for robotic fish [1,2] and other artificial swimmers [3] feature mechanisms consisting of beam-like structures in which structural travelling waves are used to induce momentum in the surrounding fluid, resulting in thrust. The same principle was effectively used in [4–6] for the design of micropumps. Both these types of nature-inspired devices use structural travelling waves and their interaction with the surrounding fluid to generate a net propulsive force: this is used either to propel the structure or to move the surrounding fluid. Artificial swimmers and micropumps, for instance, take inspiration from anguilliform locomotion which generates travelling waves from the body movement of the organism to create propulsion [7].

Travelling waves in submerged beams are utilised not only for transport devices but also for reducing drag. Research in [8] demonstrates that employing travelling waves can decrease drag by 47 % for underwater micro vehicles. For achieving high drag reduction, resonant frequency excitation should be used, reaching a maximum reduction rate of 47 %. Conversely, for net energy savings, low-frequency excitation is preferable, as it provides considerable drag reduction over larger areas while also enhancing the vehicle's endurance through energy savings.

Due to boundary conditions, beam structures inherently do not produce pure travelling waves. Adjustments in boundary conditions are necessary to suppress standing wave generation. Loh and Ro [9] introduced a two-mode excitation method using two forces positioned symmetrically along the beam length, with identical amplitude and frequency but a 90-degree phase difference. Optimal travelling waves are achieved when the beam operates between two resonant frequencies, particularly in higher modes where the hyperbolic component of the mode shape is nearly zero. This straightforward technique has been further developed in subsequent studies [10–19]. However, issues such as manufacturing precision, structural instability, and actuator discrepancies can affect pure travelling wave generation.

Kuribayashi et al. [20] proposed an alternative method based on impedance matching, utilising two actuators: one for excitation and

* Corresponding author.
E-mail addresses: Skriptyan.Syuhri@glasgow.ac.uk, Skriptyan.Syuhri@unej.ac.id (S.N.H. Syuhri).

https://doi.org/10.1016/j.ijmecsci.2024.109623
Received 14 January 2024; Received in revised form 16 July 2024; Accepted 1 August 2024
Available online 2 August 2024

another to prevent wave reflection at boundaries. This method requires precise tuning as impedance values vary with load amplitude and frequency [21]. Tanaka and Kikushima [22] introduced an active sink method, which eliminates reflecting waves at boundaries using damping mechanisms, similar to impedance matching, but effective only within specific frequency ranges.

Further developments have been made to enhance travelling wave generation. Ghenna et al. [23] proposed a vector control method to improve the two-mode excitation technique. Enhancements to the impedance matching method were achieved by adding springs to the beam ends to mitigate reflection effects [24]. Blanchard et al. [25,26] examined the addition of springs and dampers to optimise the active sink method, varying their positions for best results. Minikes et al. [27] developed a tuning method based on wave identification, enabling real-time control to achieve pure travelling waves. Furthermore, Kumar and DasGupta [28] developed a method to generate a simple harmonic travelling wave in beams using boundary excitation.

In a submerged beam without external flow, the kinetic energy of the beam is partially dissipated to the surrounding fluid through flow separation [29]. This induces a phase shift along the beam, resulting in travelling wave pattern in the vibration. Consequently, travelling waves can be produced by implementing single excitation such as a cantilever beam configuration subjected to base motion [29]. The transferred energy can be estimated from hydrodynamic forces containing an inertial force and drag force described by the Navier-Stoke equations using the numerical techniques proposed by Ahsan [30]. The inertial force aligns with the local acceleration of the beam, affecting its mass per unit length. The drag force, which is related to the local velocity of the beam, enhances the overall dissipative force acting on the beam [31]. Consequently, hydrodynamic forces typically reduce the natural frequencies and increase the damping of the beam.

Hydrodynamic forces are influenced by a variety of factors including the geometry, the fluid dynamics properties [32–34], the boundary conditions [35,36] and the velocities involved [30,37]. Sader [37] extended the study by providing correction factors for the hydrodynamic function applicable to beams with rectangular cross-sections. This methodology was further developed to examine slender beams submerged in viscous fluids, incorporating experimental verification [38], torsional vibrations [39,40], compressible fluids [41], and vibrations near solid surfaces [42,43]. It was observed that reducing the cross-section of a slender cantilever beam increases viscous damping [37]. The frequency response of a rectangular cantilever beam remains relatively unaffected by an infinite planar surface when the distance between them is greater than the beam's width [42]. When a solid surface is in close proximity to the vibrating beam, hydrodynamic loading increases significantly. Specifically, the damping component of this loading rises sharply when the Reynolds number and the ratio of the wall distance to beam width are less than or equal to one [43].

To achieve optimal design for propulsion, it is paramount to study both the qualitative and quantitative characteristics of the travelling waves generated by the beam. Here, the term "quantitative" refers to the ratio between the amplitude of the travelling wave versus the amplitude of the standing wave. This can be achieved following the technique shown in [10,44], which uses a scalar value to express how much of the displacement is caused by the travelling wave. This technique has been beneficial for extracting data from the motion of swimming fish [7,45], conducting parametric studies for system optimisation [14,15], and sensing mechanical waves [27,46]. The term "qualitative" describes the vibrational properties of travelling waves which include the amplitude, mode shapes and phase delay between the tips of the beam. Qualitative studies in travelling waves, particularly for a submerged beam, are limited in the literature. Therefore, in this paper, we extend the study of the quality of travelling waves through theoretical analysis and experimental validation.

Using validated analytical models, it is possible to explore the travelling and standing waves, and demonstrate how the travelling waves are formed. This approach is suitable to investigate the characteristics of travelling waves for each resonant frequency and determine which parameters contribute the most to the generation of travelling waves. This will enable an enhanced understanding of mechanical waves, particularly in submerged beams underwater, and contribute to the development of devices capable of generating maximum thrust with minimum effort.

This paper is structured as follows: Section 1 provides an introduction to the current applications and significance of submerged beams in liquid environments, highlighting the importance of understanding fluid-structure interactions. Section 2 covers the theoretical modelling and analysis, starting with a Galerkin-based model for fluid-structure interaction and followed by a linear approximation approach. In Section 3, we present the experimental results and analysis, describing the experimental methods, characteristics of beams in air, partially submerged in water, and fully submerged underwater, as well as the behaviour of higher modes. Section 4 focuses on model validation, detailing the validation procedure and providing results for beams with various length. Section 5 discusses the findings on linear approximation and passive travelling waves. Finally, Section 6 summarises the key contributions and implications of our study. Additional details and data are provided in the Appendix.

2. Theoretical modelling and analysis

This section explores the theoretical foundation of fluid-structure interactions involving submerged beams. It begins with introducing a Galerkin-based model for understanding the complex dynamics between the fluid and the structure. Following this, a linear approximation approach is introduced to facilitate the connection between beam displacement and the wave equation. These models establish a basis for the experimental investigations and validations presented in the subsequent sections.

The system under consideration is illustrated in Fig. 1. Due to the relative motion between the beam and base, the total displacement of the beam, $w_t(x,t)$, can be determined as follows:

$$w_t(x,t) = w_b(x,t) + w(x,t), \tag{1}$$

where t is the time, x is the position along the beam length, $w(x, t)$ is the relative (local) displacement of the clamped-free beam, and $w_b(x,t)$ is the motion of the base defined as:

$$w_b(x,t) = \delta(x) A_f \sin\omega_f t, \tag{2}$$

where $\delta(x) = 1$ for the clamped-free beam [47], $A_f$and ω_f denote the displacement and forcing frequency, respectively.

2.1. Galerkin-based model for fluid-structure interaction

The fundamental modelling assumption considers the beam as slender, where the displacement in the Z direction (refer to Fig. 1) is sufficiently small to neglect deflection in the X direction and rotational inertia. Additionally, the uniformity in flexural rigidity, EI, and mass distribution, μ, along the beam's length is presumed. For this system, the Euler-Bernoulli beam theory [48] is used. Based on the Galerkin approximation, the solution for the Euler-Bernoulli beam model can be represented as a series of independent functions containing spatial and temporal parts of the form:

$$w(x,t) = \sum_{i=1}^{\infty} \varphi_i(x) q_i(t), \tag{3}$$

where $\varphi_i(x)$ is the mode-shape of the system and $q_i(t)$ is the modal displacement for the i-th mode. The mode shape equation, $\varphi_i(x)$, is given by:

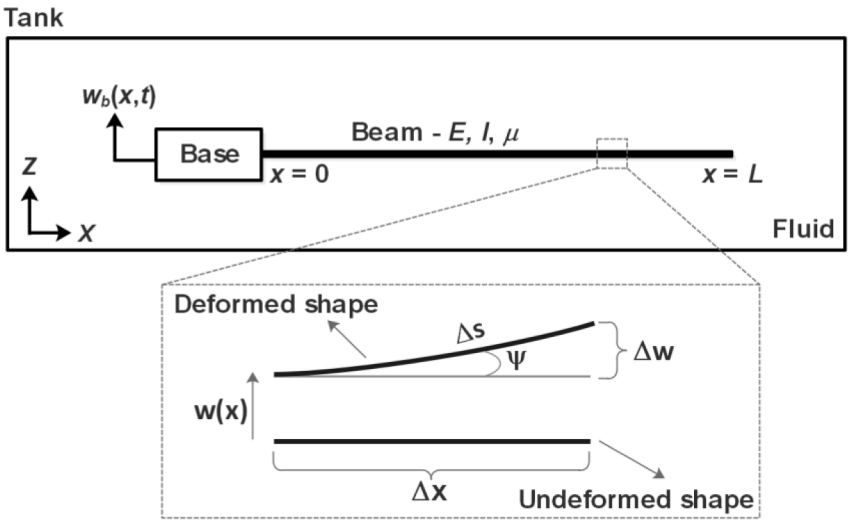

Fig. 1. Schematic diagram of the beam subjected to base excitation, along with a detailed view of a small section of the beam in its deformed position. The beam is immersed in a fluid and anchored at the base, which oscillates with a displacement $\boldsymbol{w_b(x,t)}$. The detailed view shows the deformation of the beam from its undeformed shape $\boldsymbol{w(x)}$ to its deformed shape, illustrating the changes in arc length $\boldsymbol{\Delta s}$, deflection $\boldsymbol{\Delta w}$, and horizontal distance $\boldsymbol{\Delta x}$.

$$\varphi_i(x) = \cosh\beta_i x - \cos\beta_i x - \sigma_i(\sinh\beta_i x - \sin\beta_i x), \tag{4}$$

where the values of β_i and σ_i for $i = 1, 2, \ldots, \infty$ can be obtained from [47]. The mathematical derivation leading to the mode shape equation is detailed in Appendix A.

For the case of a beam interacting with surrounding fluid, the presence of the fluid introduces two essential effects in the beam equation, namely the drag and inertial forces which can be expressed as:

$$F_f = \frac{\pi}{4}\rho_f C_m b^2 \frac{\partial^2 w}{\partial t^2} + \frac{1}{2}\rho_f C_d b \left|\frac{\partial w}{\partial t}\right| \frac{\partial w}{\partial t}, \tag{5}$$

where F_f is the total fluid force acting on the beam, ρ_f is the fluid density, b is the beam width, C_d and C_m are the drag and inertia coefficients, respectively. The expression in Eq. (5) is mainly based on the Morison equation [49] which is originally for a fixed body subjected to a fluctuating flow. Since this study considers a vibrating beam in quiescent fluid with no external flow, the flow velocity around the beam is assumed to be equal to the transverse velocity of the beam.

In this study, damping is incorporated into the Euler-Bernoulli beam equation using Eq. (5). Applying the separation of variables from Eq. (3) and multiplying by an arbitrary mode shape, with orthogonality conditions provided in Appendix A, yields the modal equation:

$$\ddot{q}_i(t) + 2\zeta_{ld,i}\omega_{ni}\dot{q}_i(t) + \frac{C_{qd}}{(\mu+M)L}\sum_{j=1}^{\infty}\sum_{k=1}^{\infty}\psi_{jki}\dot{q}_k(t)\left|\dot{q}_j(t)\right| + \omega_{ni}^2 q_i(t) = Q_i(t), \tag{6}$$

where

$$\begin{cases} Q_i(t) = \dfrac{1}{(\mu+M)L}\displaystyle\int_0^L F(x,t)\varphi_i dx = -\frac{\ddot{w}_b(x,t)}{L}\int_0^L \varphi_i(x)dx, \\ \psi_{jki} = \displaystyle\int_0^L |\varphi_j(x)|\varphi_k(x)\varphi_i(x)dx. \end{cases} \tag{7}$$

The modal coordinates in Eq. (6) are difficult to solve because it involves nonlinear differential equations due to the quadratic damping function. Therefore, a linear approximation will be used, as described in the following section.

2.2. Linear approximation

In the case of small displacement, the nonlinear term $|\partial w/\partial t|\partial w/\partial t$ in Eq. (5) can be approximated with $A_f\omega_f\partial w/\partial t$ [29]. Using the same derivation techniques, this results in a linear second order ODE analogous to a spring-mass-damper system expressed as:

$$\ddot{q}_i(t) + 2\zeta_i\omega_{ni}\dot{q}_i(t) + \omega_{ni}^2 q_i(t) = Q_i(t), \tag{8}$$

where $\zeta_i = (C_{ld} + 0.5\rho_f C_d b A_f\omega_f)/(2(\mu + M)\omega_{ni})$. This equation can be solved analytically using the Duhamel integral to obtain the solution of $q_i(t)$, as described in Appendix B.

To illustrate the wave composition in the beam, the series $lp_i\varphi_i$ and $rp_i\varphi_i$ described in Appendix B can be expressed as functions of a single wavelength as follows:

$$\begin{cases} U(\beta x) = A_f\delta(x) + \displaystyle\sum_{i=1}^{\infty} lp_i\varphi_i \cong U_1\cos\beta x + U_2\sin\beta x, \\ V(\beta x) = \displaystyle\sum_{i=1}^{\infty} rp_i\varphi_i \cong V_1\cos\beta x + V_2\sin\beta x. \end{cases} \tag{9}$$

Using trigonometric identities, this allows the beam equation to be separated based on the travelling components, resulting in:

$$\begin{aligned} w(x,t) = \frac{1}{2}&((U_1+V_2)\sin(\omega t+\beta x) + (V_1-U_2)\cos(\omega t+\beta x) \\ &+ (U_1-V_2)\sin(\omega t-\beta x) + (U_2+V_1)\cos(\omega t-\beta x)), \end{aligned} \tag{10}$$

where $(\omega t + \beta x)$ and $(\omega t - \beta x)$ represent the wave travelling in the positive and negative direction, respectively. Therefore, three possibilities of mechanical waves can be generated on the beam based on the definition of Eq. (10), namely standing, travelling and hybrid waves.

The condition of a pure standing wave emerges when damping is minimal, $\zeta \approx 0$. Consequently, $rp_i \approx 0$ or $V(\beta x) \approx 0$ as these are proportional to the damping ratio. Without V_1 and V_2, the wave in Eq. (10) propagates both positively and negatively with equal amplitudes, resulting in standing waves, often indicated by the presence of node(s) in the beam envelope, as shown in Fig. 2. The position of the node along the beam length can slightly shift left or right depending on U_1 and U_2 values.

When damping is significant, the term $V(\beta x)$ cannot be neglected. The relative contribution of V_1 and V_2 to Eq. (10) induce differences between forward travelling, $\omega t + \beta x$, and backward travelling, $\omega t - \beta x$, components, resulting in a hybrid wave pattern with a trough instead of a node, as illustrated in Fig. 2. For a pure travelling wave, it is necessary for the waves to travel solely in one direction – either positive or negative. This can be achieved by ensuring $U_1 = V_2 = 0$ and $U_2 = V_1 \neq 0$,

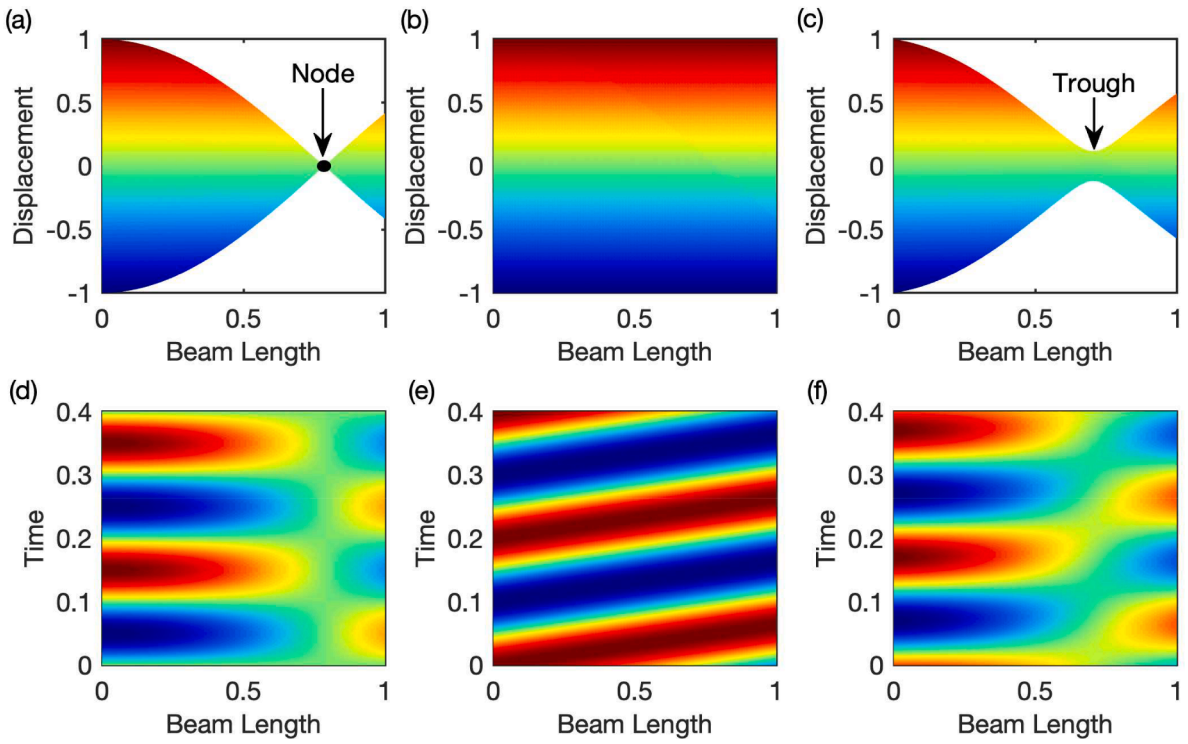

Fig. 2. Typical wave patterns in finite structures. Panels (a), (b), and (c) present the normalised displacement against the normalised beam length, highlighting different wave characteristics. In panel (a), a node is shown, representing a point of zero displacement. Panel (b) displays a uniform displacement profile along the beam. Panel (c) identifies a trough, indicating the lowest point in the displacement profile. Panels (d), (e), and (f) show the temporal evolution of the beam deflection. The colour intensity denotes the displacement magnitude, with red for maximum positive displacement and blue for maximum negative displacement. Panel (d) illustrates standing waves with nodes, while panel (e) shows travelling waves propagating in one direction. Panel (f) features hybrid waves characterised by troughs.

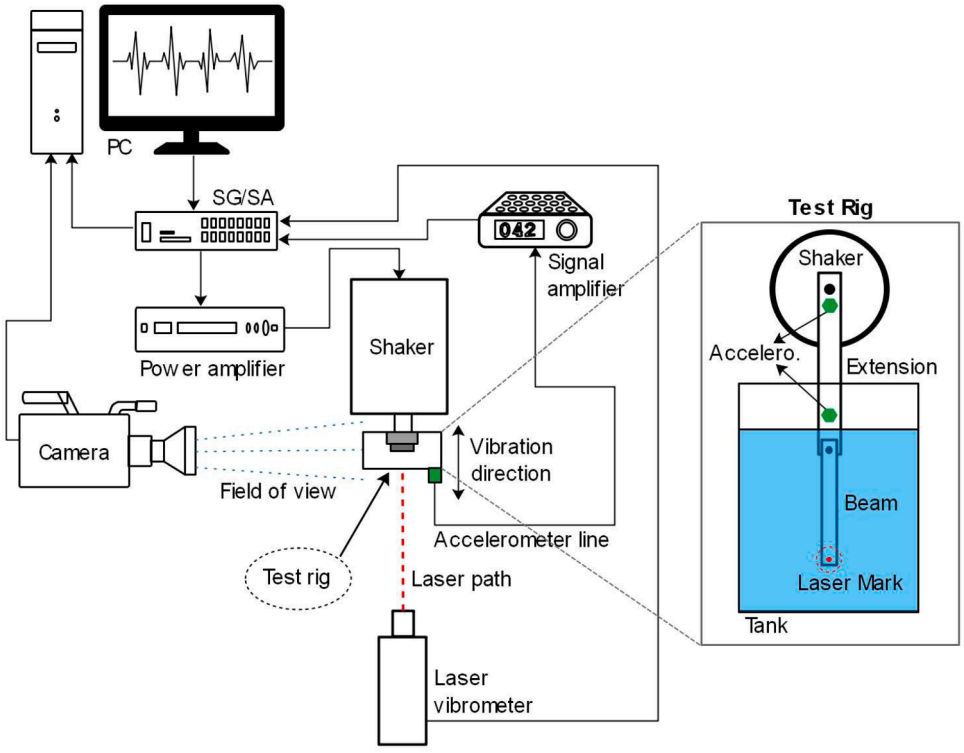

Fig. 3. The general layout of the experimental setup. The system includes a PC for data acquisition, a signal generator/signal analyser (SG/SA), a power amplifier, and a shaker to induce vibrations in the beam. The beam is submerged in a tank, and its vibrations are measured using accelerometers and a laser vibrometer. A camera captures the movement of the beam. The detailed section on the right shows the placement of the shaker, accelerometer, and beam within the tank.

causing the wave equation in Eq. (10) to simplify to $\cos(\omega t - \beta x)$. In practice, this involves adjusting boundary conditions to eliminate reflecting waves, as outlined in references [20–22,50].

3. Experimental results and analysis

This section presents the experimental procedures and results, aiming to empirically validate the theoretical models discussed earlier. The experimental methods used to characterize the beams' behaviour in different environments— in air, partially submerged in water, and fully submerged underwater—are described in detail. The analysis includes the evaluation of higher vibrational modes, providing a comprehensive understanding of the beam dynamics under varying conditions.

3.1. Experimental methods

Experimental validation is essential for verifying the accuracy and assessing limitations of derived analytical models, particularly by obtaining properties and dynamic responses of the beam. Beam properties are examined via prescribed frequency response function (FRF) measurements to determine natural frequencies and damping factors. These parameters are crucial for determining simulation parameters for validation as well as comprehending how the surrounding fluid influencing the behaviour of the beam. By exploring the dynamics of the beam with respect to time (t) and length (x), a comprehensive comparison and examination of the experimental and analytical models is carried out.

The schematic diagram of the experimental setup is illustrated in *Fig. 3*. A PC was used to visualise the data and provide an interface to the signal generator, signal analyser (SG/SA), and high-speed camera. The output from the signal generator was amplified by a 48-W power amplifier, LDS PA25E, and then channelled into an electrodynamic shaker, LDS V201, to induce vibrations. To enable complete immersion, the beam was constrained to the moving platform of the shaker through an extension (supporting) plate so that the beam would be completely submerged within a water-filled tank (see *Fig. 3*). The tank had dimensions of 15 cm in diameter and 28 cm in height and was mounted on an adjustable table to allow variation in the beam's immersion depth. The supporting plate, acting as a rigid constraint for the beam, was designed to yield a first natural frequency of approximately 130 Hz. This value was intentionally set nearly three times higher than the operational frequency of the beam to prevent any dynamic interaction between resonances.

As shown in Fig. 3, one accelerometer was located at the connection between the extension and shaker to measure the input acceleration from the shaker, and a second accelerometer was placed close to the beam. These two accelerometers served to detect any additional dynamics introduced by the extension that might impact the motion of the beam. The accelerometers used were ceramic shear accelerometers from PCB Piezotronics, specifically Model-352C22, with signals amplified using a PCB Piezotronics Model-428C signal amplifier. A Polytec PDV100 laser vibrometer was directed toward the free tip of the beam, targeting the laser reference point indicated in *Fig. 3* to measure the beam's velocity. To estimate the FRF of the system, the output signals from the sensors were connected to the SignalCalc Ace signal analyser, powered by the Quattro hardware platform.

The motion of the beam was captured using a Photron Fastcam SA1.1 high-speed camera set at a 2000 fps frame rate and 1/2000s shutter speed. A sample image is displayed in Fig. 4(a). This image was converted to binary using MATLAB's "edge" syntax with the Canny method, rendering the beam edge as white pixels and the rest as black (*Fig. 4*(b)), where only a portion of the binary image is shown for editorial reasons. After successful conversion to a logical image (black = 0, white = 1), coordinates of non-zero (white) pixels were collected. This generated a one-dimensional array plotted in Fig. 4(c), where the X-Y position of the beam is displayed for a given instant of time.

Using the same methodology on a series of images captured consistently over time, 3D vectors containing beam length, time and beam displacement in the x-, y- and z-directions were obtained. An illustration of this data acquisition is shown in Fig. 5: it is worth mentioning that the *X Pixel* direction in Fig. 4(a) is aligned with the z-directions in Fig. 5, and the *Y Pixel* direction in Fig. 4(a) is aligned with the x-directions in Fig. 5. Two essential projections are employed: the xz- and xy-plane. The xz-plane, representing the front view, displays the beam envelope's projection with respect to its length, while the xy-plane presents the contour displacement with respect to t and x. For enhanced comparison with the analytical model, the beam length is normalised against L and the beam displacement is normalised against the maximum displacement value at $x = 0L$.

For small displacements, post-processed data might exhibit noise from factors such as the anti-aliasing filter of the camera and edge detection algorithm filtering. This can introduce inconsistent pixel movement in the pixel grid over time. Thus, for the DIC measurements, the input frequency and amplitude were chosen so that beam

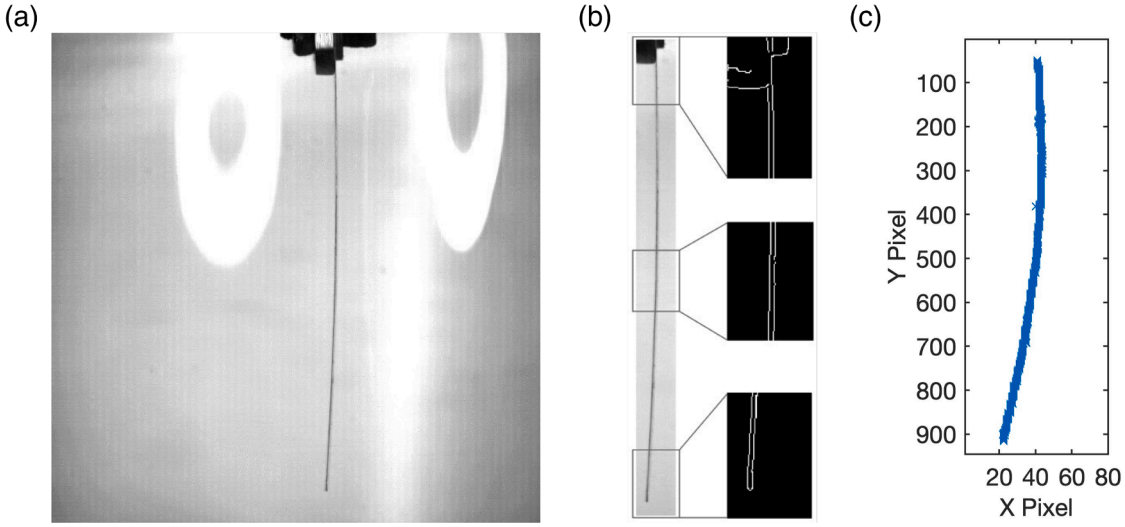

Fig. 4. (a) A sample image of a fully submerged beam taken by the high-speed camera, (b) Conversion from a true colour image to a binary logical image, with detailed views showing the conversion process at different sections of the beam. (c) Pixel coordinates extracted from the binary image, illustrating the deflection of the beam.

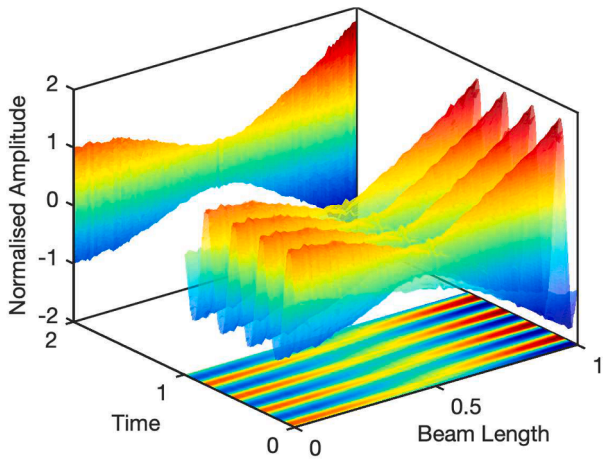

Fig. 5. A 3D-plot of the normalised displacement with respect to the normalised beam length and time. This plot is created from a series of experimentally captured images and converted into contour data. The colour intensity indicates the magnitude of displacement, with warmer colours representing higher displacement values.

displacements larger than 1 mm were obtained; with our excitation system, this was possible in the frequency window of 0–50 Hz.

3.2. Beam characteristics in air

The beam used in this investigation was characterised by specific dimensions: a length, width and thickness of 80 mm, 12.75 mm, and 0.08 mm, respectively. The material density was determined to be approximately 7200 kg/m^3. The experimental setup depicted in Fig. 3 was modified to obtain the beam characteristics in air, and the water tank was removed. A random signal generated by the SG/SA was used to generate white noise across the range of frequencies 0–250 Hz to obtain the FRF of the beam. Three maximum amplitude levels have been used: 80 mV, 200 mV and 300 mV. As displayed in Fig. 6, the resulting FRF depicts the beam tip velocity relative to the base acceleration for the three different amplitude levels.

At the first natural frequency shown in Fig. 6(a), it can be observed that the peak decreases and experiences a slight shift with increasing amplitude. This relatively weak nonlinearity is likely attributable to the interaction between the beam and the surrounding air medium [51]. Nonlinear behaviour also becomes evident near the second natural frequency, as shown in Fig. 6(b). This anomaly is characterised by a notch-like feature.

Fig. 6(c)-(e) shows the steady-state vibration of the beam in air for various frequencies. In the first row of the figure, the displacement of the beam is projected onto the time-beam's length plane (t vs x). The second row illustrates the displacement projection versus the beam's length, x, as described in Fig. 5. The plots in Fig. 6(c)-(e) demonstrate mechanical waves characterised by relatively low damping values mainly due to air resistance and material properties. It is important to note that in Eq. (B.1), low damping values result in vanishing rp_i terms. In good approximation, the cosine term of the equation can be neglected, and the solution converges to the standing wave solution of the beam equation. This phenomenon can also be interpreted using Eq. (9), where low damping values lead to negligible $V_i(x)$ terms and ultimately cause the waves to travel (propagating) in the positive and negative directions equally, hence generating standing wave formation.

The beam envelope at $f = 8$ Hz, shown in Fig. 6(c), can be described as the sum of the base amplitude and the first mode shape. This can be approximated using Eq. (B.2) with the spatial function $U(\beta x) = (A_f + lp_1\varphi_1)$. At $f = 14$ Hz, displayed in Fig. 6(d), despite lying between the first two resonant peaks, the influence of the second mode remains relatively small. The nodal point appears because $(\omega_{n1}^2 - \omega^2)$ turns negative when $\omega > \omega_{n1}$ resulting in a negative value of lp_1.When $lp_1\phi_1 + lp_2\phi_2 = -A_f$, $U(\beta x)$ reaches zero. Therefore, all the coefficients $U_i$of the spatial function of the wave equation become zero – the coefficient V_i are close to zero due to the low value of damping – resulting in a node in the motion of the beam. By increasing the forcing frequency, the influence of the second mode becomes more pronounced, causing the nodal points to shift towards the free end of the beam. This phenomenon is evident in Fig. 6(e) when the beam is actuated at $f = 40$ Hz, which falls between the first and second resonant peaks but closer to the second natural frequency.

The identification of the stiffness and damping coefficients uses the transient (decay) responses of the system in free vibration following the nonlinear identification method devised by Londono [52]. This approach investigated the nonlinear behaviour, particularly due to the presence of the notch in the FRF observed in the second resonant frequency. This method enabled the extraction of the nonlinear backbone and damping curves. It relies on tracking the peak and zero-crossing points to estimate the instantaneous amplitude and frequency. A harmonic input signal is applied to the beam at a specific modal frequency to give an accurate estimation. The forcing is maintained until the system attains a steady state, at which the input signal is abruptly terminated. Consequently, the beam enters a free vibration phase within the designated mode, effectively eliminating any influence from the other modes. This technique is commonly known as the resonance decay method [53].

The noise in the measurements was mitigated through the use of a band-pass filter, and the data point was interpolated using linear interpolation to facilitate the smooth detection of zero-crossing points, avoiding errors introduced by irregular measurement. Fig. 7(a) and (b) show the backbone and damping curves, respectively, for the first mode, where the instantaneous frequency and damping curves were smoothed using a 10-point (symmetric) moving average filter. As expected, both curves display amplitude dependency. Given the frequency range in which the backbone curve varies, this can be considered in good approximation linear. Conversely, the damping curve exhibits a positive gradient, confirming the quadratic relation used in the theoretical description of the damping in Eq. (5).

Unlike the first mode, the second resonance shown in Fig. 7(c) and (d) presents a notable discontinuity in both the backbone and damping curves. At this frequency, the beam's vibrations are relatively small, and the impact of air damping on the structure is minimal. However, when the forcing amplitude is increased, as exemplified at 5 mV, an intriguing phenomenon arises: after the force is discontinued, the accelerometer positioned at the tip of the supporting plate captures vibration signals. Frequency-domain analysis reveals that both the beam and the supporting plate decay at the same frequency. This suggests that the beam interacts with the supporting plate in a manner reminiscent of a dynamic vibration absorber. This interaction is the underlying reason behind the discontinuity observed in the backbone and damping curves illustrated in Fig. 7(c) and (d), and the FRF of the second mode shown in Fig. 6(b). Overall, this observation supports the assumption that damping due to air and material properties only contributes minimally to damping ratio, $\zeta < 0.8\%$, as inferred from the damping curves in Fig. 7.

3.3. Characteristics of beam partially submerged in water

This section investigates the behaviour of the beam when partially submerged, providing insight into the transition effects between the air and water environments. These experiments are crucial for understanding the initial stages of submersion and the interaction of the structure with the fluid at varying depths. Although numerous studies have explored into the behaviours of partially submerged beam in water [54–62], the propagation of structural travelling waves in such conditions remains largely uncharted. This study aims to illuminate this

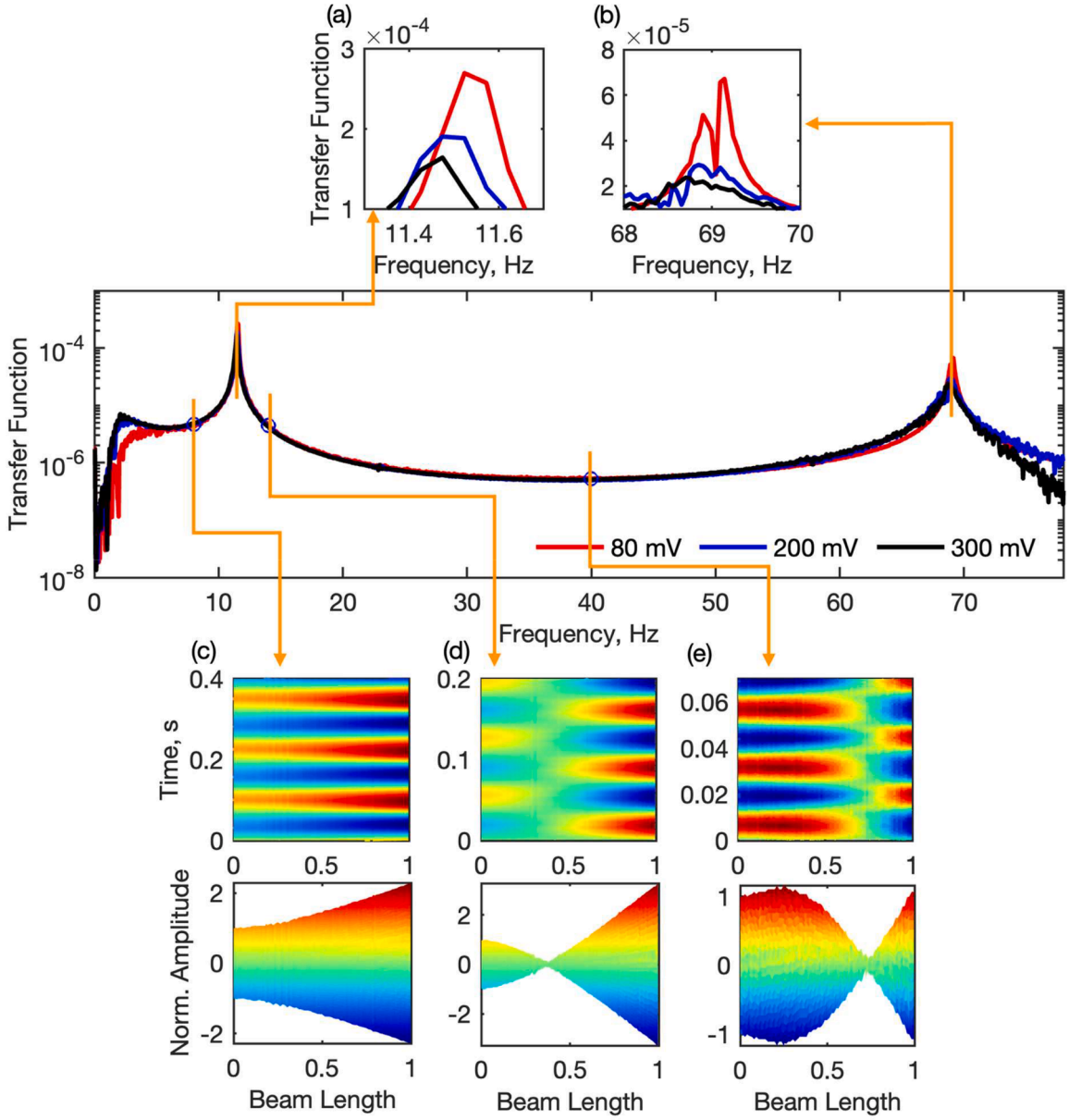

Fig. 6. FRF (Frequency Response Function) of the beam in air for various amplitudes. The main plot shows the transfer function across a range of frequencies for three different input amplitudes: 80 mV (red), 200 mV (blue), and 300 mV (black). Insets (a) and (b) display zoomed sections of the first and second peaks, respectively, highlighting detailed frequency responses. Panels (c), (d), and (e) illustrate the steady-state beam responses generated with forcing frequencies of 8 Hz, 14 Hz, and 40 Hz, respectively. The upper part of each panel shows the temporal evolution of the beam deflection, and the lower part shows the corresponding normalised amplitude along the beam length. Blue circle markers in the main plot indicate the locations of the forcing frequencies in the FRF.

phenomenon offering valuable insights to enhance the existing models.

Fig. 8 shows the FRF of the beam tip relative to the base acceleration for various dipping depths, denoted with d. These FRFs are obtained through the application of a random signal characterised by a maximum amplitude of 100 mV. It is worth noting that the relatively low signal-to-noise ratio observed in the proximity to the first peak is likely due to the accelerometer's cut-off frequency. The figure provides a visualisation of how the position of the second peak rapidly shifts toward lower frequencies with increasing the dipping depth, progressing from 1 cm to 5 cm. Notably, after approximately two-thirds of the beam is submerged in water, there is only a marginal change in the position of the second peak. This is highlighted by the black and green lines in the FRF shown in Fig. 8. At a dipping depth of $d = 5$ cm, the emergence of the third mode becomes visible at a frequency just below 60 Hz. Furthermore, at a dipping depth of $d = 7$ cm (indicated by the green line), the third resonant frequency becomes more prominent and, surprisingly, aligns with the second mode observed at a dipping depth of $d = 1$ cm (depicted by the red line).

To explore the steady-state vibration of the beam, a dipping depth of $d = 5$ cm was selected for further analysis. The findings of this investigation are presented in Fig. 8, which showcases a contour plot of the beam at the specified dipping depth while considering various forcing frequencies. The techniques used to obtain these responses requires the correction for the change of refractive index between air and water, as described in Appendix C.

From inspection of Fig. 8(a), it can be observed that at a forcing frequency of $f = 4$ Hz, near the first mode, a node is visible around the boundary of the air and water interface. As the forcing frequency increases to 8 Hz, shown in Fig. 8(b), the node tends to migrate towards the free end of the beam. This phenomenon is consistent between the

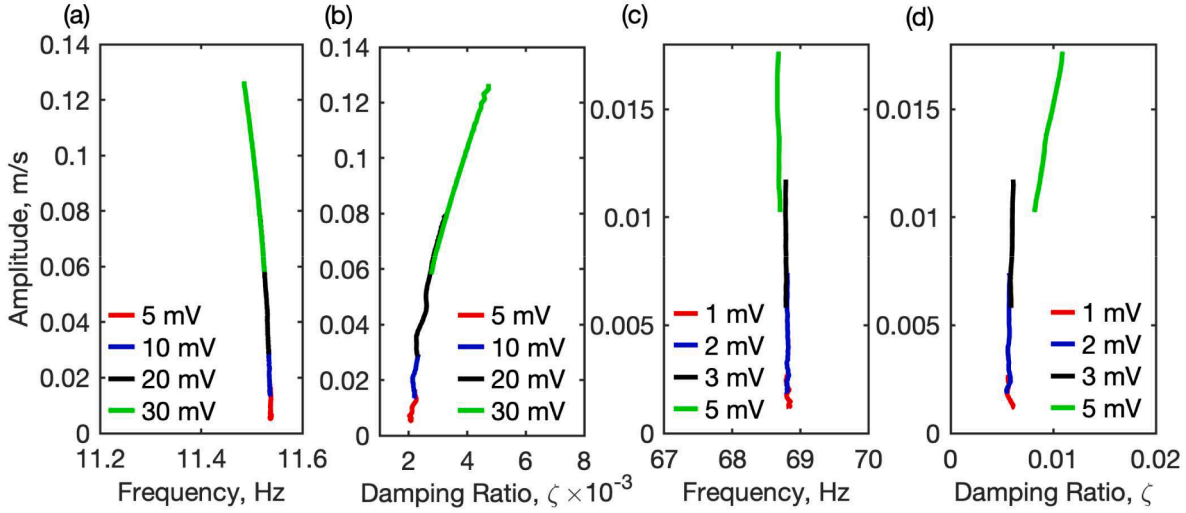

Fig. 7. (a) Backbone and (b) damping curves of the first natural frequency, and (c) backbone and (d) damping curves of the second resonant frequency. The amplitude of vibration (m/s) is plotted against frequency (Hz) and damping ratio (ζ) for various input voltages. Panels (a) and (b) illustrate the response at the first natural frequency with input voltages of 5 mV (red), 10 mV (blue), 20 mV (black), and 30 mV (green). Panels (c) and (d) show the response at the second resonant frequency with input voltages of 1 mV (red), 2 mV (blue), 3 mV (black), and 5 mV (green).

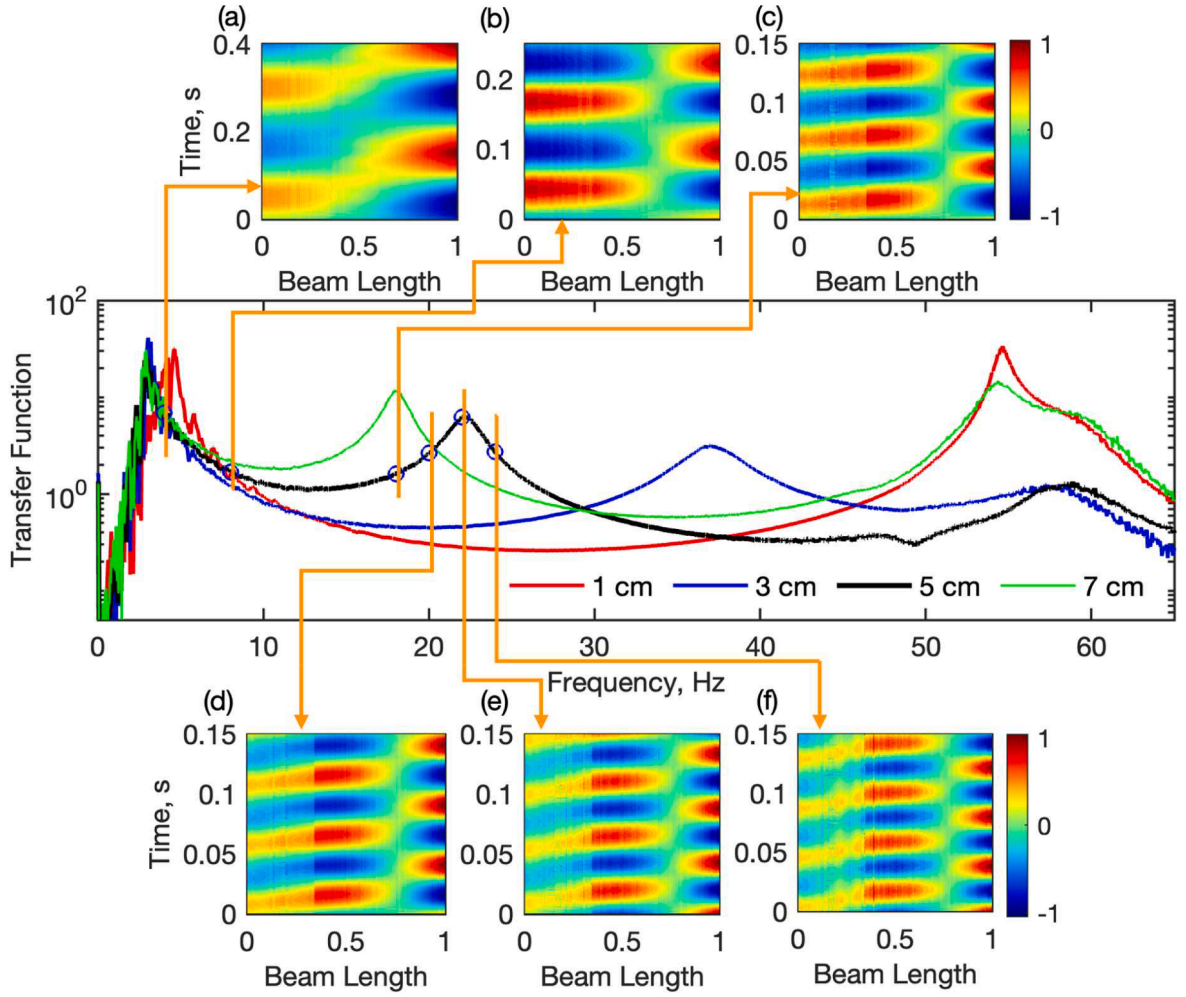

Fig. 8. Influence of the dipping depth on the beam FRF. The main plot shows the transfer function across a range of frequencies for different dipping depths: 1 cm (red), 3 cm (blue), 5 cm (black), and 7 cm (green). Panels (a) to (f) display the vibration responses of the partially submerged beam with a dipping depth of 5 cm, generated with forcing frequencies of 4 Hz, 8 Hz, 18 Hz, 20 Hz, 22 Hz, and 24 Hz, respectively. Each panel shows the temporal evolution of the beam deflection along the beam length, and the blue circle markers in the main plot indicate the locations of the forcing frequencies in the FRF.

beam vibrating in both air and water. Upon exceeding the threshold of 16 Hz, which marks the lowest magnitude point in the FRF between the two peaks, the dry part of the beam, shown in Fig. 8(c), manifests travelling waves. This wave behaviour, displayed in Fig. 8(d), intensifies as the frequency reaches 20 Hz, signifying the presence of strong travelling waves within the structure. After passing the second peak, observed at $f = 22$ Hz in Fig. 8(e), the wave speed in the dry part of the beam further increases, while in the submerged section it remains relatively constant.

Notably, at $f = 24$ Hz, shown in Fig. 8(f), slightly beyond the second peak, the emergence of a second node becomes apparent in the transition region between the air and water interfaces. It is important to note that a small base excitation around the second mode can lead to a substantial tip displacement. This is captured by the pronounced difference in colour intensity between the dry and wet portions of the beam.

The phenomenon in Fig. 8 is better approximated with a simple model described in references [26,46]. This model involves an elastic structure coupled with a spring-dashpot system positioned at one location along the structure's length. The spring and dashpot prevent reflecting waves from propagating along the structure. Consequently, there exist segments of the structure which exhibit pure travelling waves, and others predominantly standing waves.

3.4. Characteristics of beam fully submerged underwater

Using the procedures described in Section 3.1, Fig. 9 displays the FRF of the fully submerged beam for various excitation amplitudes. The second and third peaks exhibit a consistent pattern: as the forcing amplitude increases, the magnitude at the resonant peak decreases. This noticeable trend suggests the presence of a strong nonlinear damping function that depends on the amplitude of vibration.

In theory, the relationship between natural frequencies in air and water can be expressed as follows [63]:

$$f_{n,w} = f_{n,a}\left(1 + \frac{\pi\rho_w b}{4\rho_b h}\right)^{-1/2}. \tag{11}$$

Substituting the first-two natural frequencies acquired from the tests conducted in air into Eq. (11) yields the first and second natural frequencies of 2.69 Hz and 16.88 Hz, respectively. The estimated values for the second natural frequency falls below the damped natural frequencies observed in the measurements in Fig. 9. This discrepancy can potentially be attributed to the effect of the surrounding fluid on the flexural rigidity, EI: this will be further investigated in Section 4.

Fig. 9(a)-(f) illustrates the vibration responses of the beam across various forcing frequencies. At $f = 4$ Hz, shown in Fig. 9(a), the colour map indicates that the node is located at the midpoint of the beam. Approaching the second peak, as indicated at $f = 16$ Hz in Fig. 9(b), a

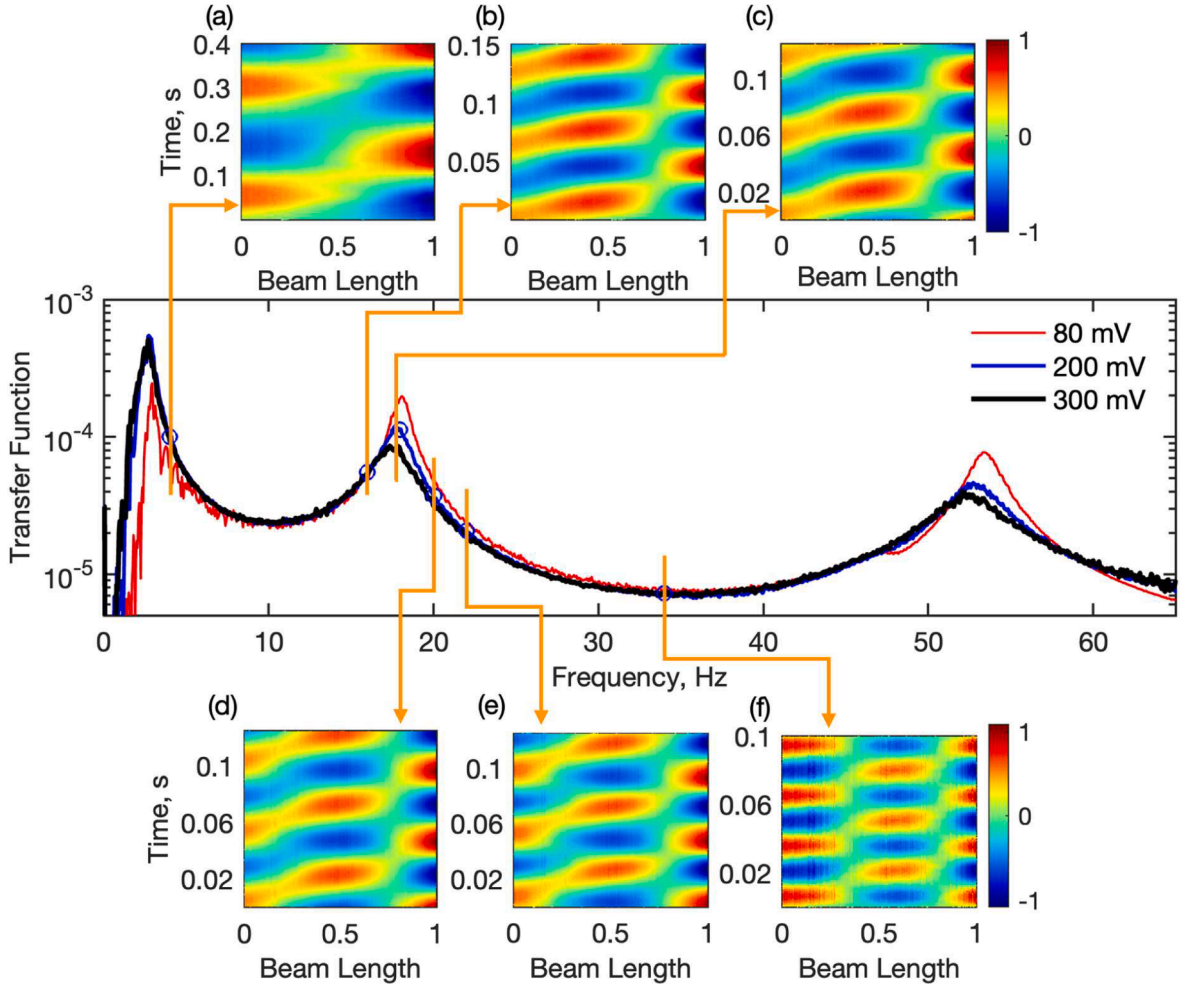

Fig. 9. Measured FRF of the beam fully submerged underwater. The main plot shows the transfer function across a range of frequencies for different input amplitudes: 80 mV (red), 200 mV (blue), and 300 mV (black). Panels (a) to (f) display the vibration responses of the partially submerged beam with a dipping depth of 5 cm, generated with forcing frequencies of 4 Hz, 16 Hz, 18 Hz, 20 Hz, 22 Hz, and 34 Hz, respectively. Each panel shows the temporal evolution of the beam deflection along the beam length, and the blue circle markers in the main plot indicate the locations of the forcing frequencies in the FRF.

clear travelling wave phenomenon becomes evident, characterised by the increased inclination of the colour contours, which indicate a higher wave speed. However, there is a noticeable discontinuity in the wave pattern attributed to the presence of the node associated with the second mode shape. After reaching the second peak, the mechanical waves transition from a single-node into a dual-node configuration, while maintaining their travelling waves nature. These transitions are effectively captured in Fig. 9(c)-(e) within the range of $f = 18$ Hz to $f = 22$ Hz.

Furthermore, as the frequency reaches $f = 34$ Hz, depicted in Fig. 9 (f), the second node attains full formation, and the standing waves dominate the beam dynamics. This observation suggests that travelling waves manifest in close proximity to the natural frequencies, while standing waves become apparent when the forcing frequency is tuned away from these resonant points.

3.5. Higher modes

Artificial swimmers and micropumps use travelling waves on higher

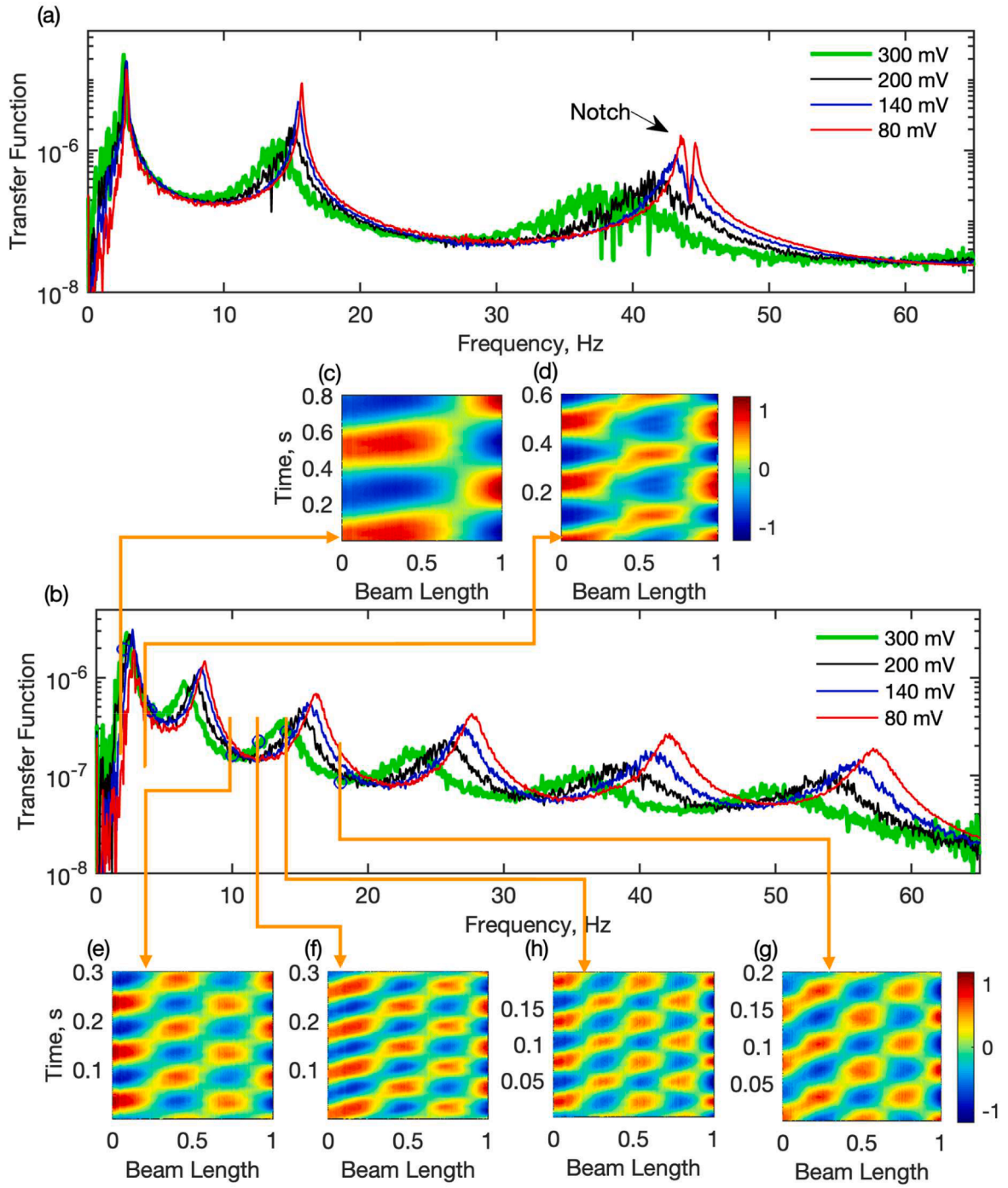

Fig. 10. FRF of the submerged beam in (a) air and (b) fully immersed underwater. The main plots show the transfer function across a range of frequencies for different input amplitudes: 80 mV (red), 140 mV (blue), 200 mV (black), and 300 mV (green). Panels (c) to (h) display vibration patterns of the submerged beam actuated with forcing frequencies of 2 Hz, 4 Hz, 10 Hz, 12 Hz, 14 Hz, and 18 Hz, respectively. Each panel shows the temporal evolution of the beam deflection along the beam length. The blue circle markers in the main plots indicate the locations of the forcing frequencies in the FRF. The notch in panel (a) is similar to the one observed in Fig. 6.

modes rather than operating within lower modes. To generate this motion, an investigation was conducted on a metal beam characterised by a length, width and thickness of 135 mm, 12.75 mm, and 0.04 mm, respectively. Fig. 10(a) and (b) presents the FRF of the elastic beam both when in air and fully submerged in water for various amplitudes. Using the quadrature peak-picking method, it was found that this beam is considerably damped compared to a beam with higher thickness values.

The notch observed in the third resonance shown in Fig. 10(a) is similar to the phenomenon observed in Fig. 6(b). In Fig. 6(b), the beam interacts with the supporting plate that mimics the behaviour of a

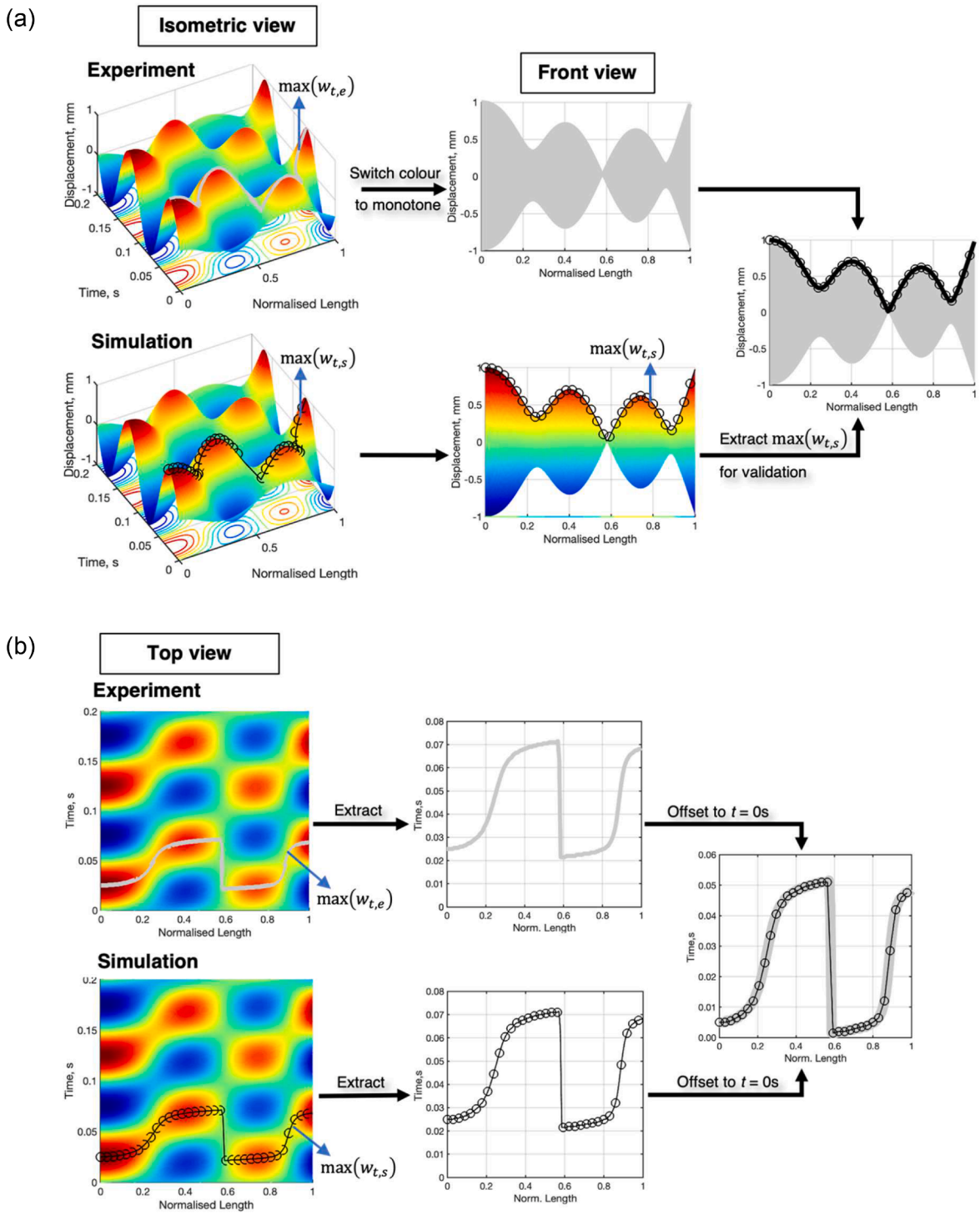

Fig. 11. Schematic diagram of validation between experiment and numerical simulation: (a) beam envelope, and (b) maximum displacement against $\boldsymbol{x}$ and $\boldsymbol{t}$. In (a), the front view highlights the maximum displacement $\max(\boldsymbol{w_{t,e}})$ from the experiment and $\max(\boldsymbol{w_{t,s}})$ from the simulation, with colour switching to monotone for clarity. The extracted maximum displacement is used for validation. In (b), the top view shows the time evolution of the beam's displacement along its length for both the experimental (top) and simulation (bottom) results. The extracted data highlights the maximum displacement, which is compared by offsetting to $\boldsymbol{t} = 0\boldsymbol{s}$. The graphs on the right depict the maximum displacement profiles against normalised length and time for both the experiment and simulation, facilitating direct comparison and validation.

dynamic vibration absorber. This interaction is the fundamental reason for the discontinuity observed in the backbone and damping curves depicted in Fig. 7(c) and (d). Moreover, it is essential to note that this notch disappears when the beam is tested underwater as shown in Fig. 10(b). Given the substantial damping provided by the liquid environment, the notch is not expected to affect the main response. Furthermore, our experiments utilise a maximum forcing frequency that is two times less than the frequency at which the notch appears. Consequently, this notch does not interfere with the primary response of the system and should not be a cause for concern in this study.

In the underwater experiments illustrated in Fig. 10(b), it is important to highlight that the first mode, estimated using Eq. (11), falls below 1 Hz, surpassing the accelerometer's cut-off frequency. Consequently, the first peak evident in Fig. 10(b) pertains to the second resonant frequency. As anticipated, there are four modes under 20 Hz, making the beam the best candidate for effectively emulating anguilliform locomotion.

Fig. 10(c)-(g) visually represents the wave propagation with respect to time and length, achieved by setting the signal generator to a maximum amplitude of 300 mV. Notably, the beam transitions from one node to three nodes below 10 Hz. Examining Fig. 10(e)-(h), the plots from $f = 10$ Hz to $f = 14$ Hz offer insights into mechanical wave formation around the fourth resonance. Strong travelling waves are evident at $f = 12$ Hz. The fourth node appears as the frequency reaches $f = 14$ Hz, indicating progression beyond the fourth peak. By $f = 18$ Hz, shown in Fig. 10(g), the fourth node is fully established.

4. Model validation

This section focuses on validating the theoretical models using experimental data. The validation procedure is outlined, detailing the steps taken to ensure the models accurately represent the observed behaviour of the beams. Validation results for beams of two different lengths, 8 cm and 13.5 cm, are presented to demonstrate the robustness of the models across varying conditions. This validation provides valuable insights into the applicability of the theoretical approaches developed in Section 2.

4.1. Validation procedure

It is important to emphasise that the validation process focuses on steady-state responses. In Section 2, the beam's motion was theoretically by separating the spatial and temporal contribution. To validate the spatial function, a comparison between the beam envelope of the experimental observations and simulations is carried out. Fig. 11(a) shows a schematic of the procedure used to compare the numerical and experimental beam envelope at a specific frequency. The envelopes, denoted as $\max(w_{t,e})$ and $\max(w_{t,s})$ for the experiment and simulation respectively, are obtained by tracking the maximum amplitudes of the displacement along the beam length. For each location along the beam length, the algorithm finds the value of the first maximum in the time series – which will be the same over subsequent periods since the response of the beam is in a steady state.

Fig. 11(b) presents the procedure used to track the maximum displacement over time, comparing the experimental and numerical maxima, thereby validating the behaviour of the temporal function used to describe the displacement of the beam. It is worth noting that the discontinuity observed at $x = 0.5L$ due to the presence of a node or trough complicates the characterisation of the waves, as it splits the spatial domain into distinct regions.

4.2. Beam with $l = 8$ cm

Before comparing the responses of the analytical and experimental models, it is necessary to identify the correct nonlinear damping model in terms of the modal coordinate, $q_i(t)$. This requires an estimation of the mechanical parameters used in the underlying linear beam model (i.e., the model of the beam when the nonlinear interaction with the water is not present). For this purpose, the flexural rigidity, EI, has been estimated by substituting the first and second resonant frequencies obtained from the experimental results in air into the formula for natural frequencies derived from the Euler-Bernoulli beam model. This yielded values of EI equal to 7.64×10^{-6} N m^2 and 6.95×10^{-6} N m^2 for the first and second modes, respectively. The average of these values, 7.23×10^{-6} N m^2, has been used in the model. With the linear parameters identified, the nonlinear coefficient values outlined in Eq. (A.6) can be calculated numerically, and the results are provided in *Table 1*.

From *Table 1*, it is evident that the values of the modal cross-coupling terms, such as Ψ_{121},Ψ_{211},Ψ_{221},Ψ_{121}, Ψ_{122} and Ψ_{221}, are small in comparison to Ψ_{111} and Ψ_{222}. Therefore, only the modal terms with $i = j = k$ are considered, reducing the overall complexity of the proposed formulation. Eq. (A.6) is a nonlinear second-order differential equation that cannot be solved analytically; hence, it was solved using the numerical integration scheme Runge-Kutta Prince Dormant (ode45 in MATLAB), leading to solutions for $q_1(t)$ and $q_2(t)$ that encompass both transient and steady-state components. To permit the comparison between the numerical models and experimental measurements, the transient responses have been eliminated.

For numerical simulation, the water density ρ_f is set to 997 kg/m^3, while the coefficients C_m and C_d are 1 and 1.8 respectively, according to references [3,64]. Fig. 12(a) provides a comparison between the experimental and nonlinear analytical models generated at $f = 4$ Hz. The envelope of the analytical model, displayed using a black solid line in Fig. 12(a), is superimposed on the experimental results, shown in monotone grey. For clarity, the contour map of the analytical model in Fig. 12(b) highlights the pattern followed by the maximum displacements in the time-beam length plane, with the black line illustrating the beam envelope. Note that the wave propagation contour map for the experimental results is presented in Fig. 9. Examining Fig. 12(b), it becomes evident that the maximum amplitude at $x = 0L$ occurs at $t = 0.06s$ – depending solely on the time needed for the transient to pass. To simplify the comparison with the experimental data, an offset in time was introduced to align the wave propagation for both models so that they both start at $t = 0s$, as illustrated in Fig. 12c). In general, the comparison of spatial and temporal functions against the experimental measurements yields satisfactory results.

Applying a similar methodology, the responses in Fig. 12(d)-(f) were generated for $f = 16$ Hz. Noticeably, the envelope of the analytical model, depicted with the black line in Fig. 12(d), exhibits slight variations, particularly in terms of amplitude and location of nodes, when compared to the experimental model. Conversely, the wave propagation shown in Fig. 12(f), aligns well for both models. This suggests that the discrepancies may arise due to parameters associated with the damping and the spatial functions. Note that the damping estimation used in this study is based on the Morison equation, originally formulated for a fixed cylinder body within an oscillatory flow: as reported in [29]. This approach can lead to damping underestimation for large vibration amplitude, as demonstrated in references [33,65,66], the hydrodynamic forcing functions which are related to the coefficients C_m and C_d in

Table 1
Nonlinear coefficient values of Eq. (A.6).

jki	$\lvert\ddot{q}_j\rvert\ddot{q}_k$	ψ_{jki}
111	$\lvert\ddot{q}_1\rvert\ddot{q}_1$	0.118225
121	$\lvert\ddot{q}_1\rvert\ddot{q}_2$	−0.03196
211	$\lvert\ddot{q}_2\rvert\ddot{q}_1$	0.079282
221	$\lvert\ddot{q}_2\rvert\ddot{q}_2$	−0.00707
112	$\lvert\ddot{q}_1\rvert\ddot{q}_1$	−0.03196
122	$\lvert\ddot{q}_1\rvert\ddot{q}_2$	0.076415
212	$\lvert\ddot{q}_2\rvert\ddot{q}_1$	−0.00707
222	$\lvert\ddot{q}_2\rvert\ddot{q}_2$	0.103617

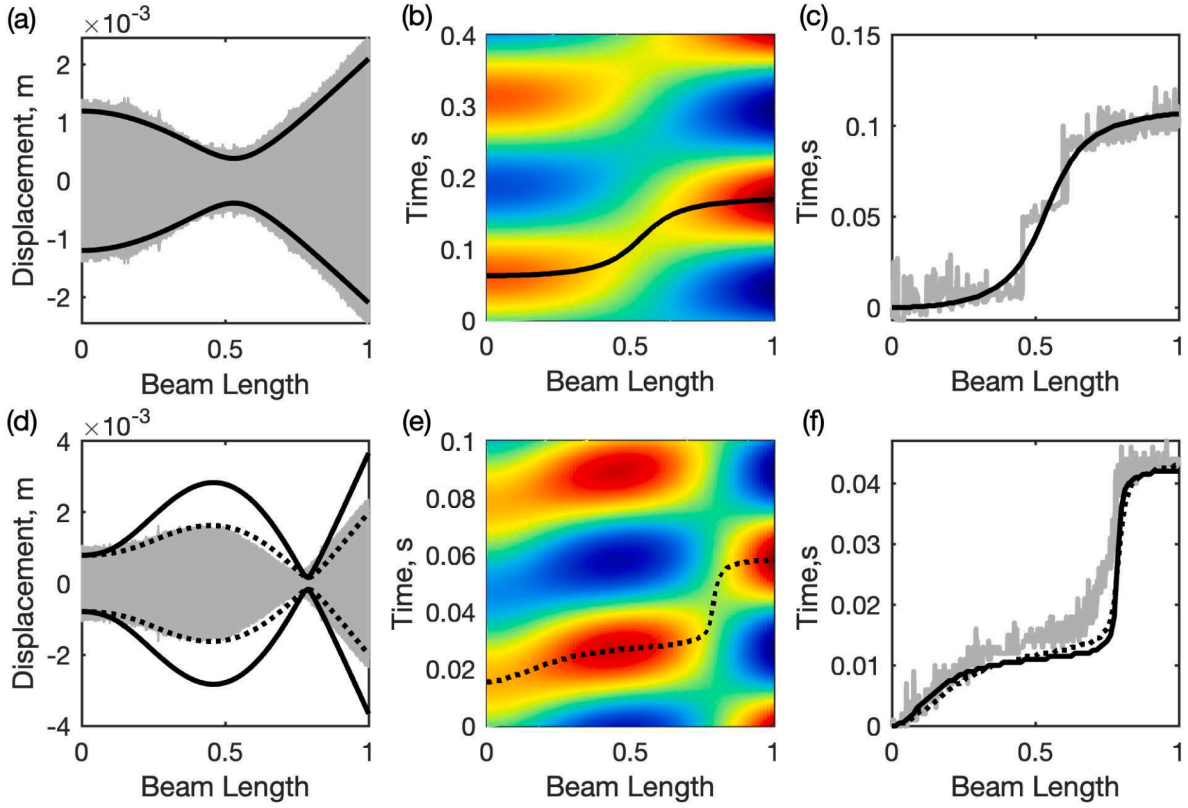

Fig. 12. Comparison of the analytical and experimental models. (a), (b), and (c) were generated at 4 Hz and (d), (e), and (f) were actuated at 16 Hz. The grey line indicates the experimental model. The solid black lines represent the numerical model, and the dotted black lines indicate the numerical model with modified C_d. The envelope line and contour map in the second column refer to the analytical model. Panel (a) shows the displacement along the beam length, (b) depicts the time evolution of the displacement of the beam, and (c) compares the time evolution between the experiment and simulation. Panels (d), (e), and (f) follow the same format for the higher frequency. The comparisons highlight the agreement and differences between the experimental and numerical models.

Morison's equation vary depending on vibration amplitude and frequency. For the case of a flat plate subjected to large vibration amplitude induced by an oscillatory flow, Aureli et al. [65] observed that the C_d value can fall within the range of 0.5 to 4.2. Hence, in this study, a parametric investigation of C_d was conducted: it was found that to produce the best fit for the experimental result, the Morrison value of C_d needs to be multiplied by a correction factor of 2. As seen in Figure 12(f), the use of the correction factor does not substantially alter the responses over time and beam length.

Fig. 13 shows a comparison between the two models for forcing frequencies ranging between the second and third resonant frequencies. The first three modes were employed in the numerical simulations, with a nonlinear coefficient value ψ_{333} of 0.101934. Specifically, Fig. 13 a) and (c) present the superposition of the experimental and numerical results at $f = 18$ Hz. For generating steady-state responses from the numerical simulation at $f = 22$ Hz, depicted in Fig. 13 (d)-(f), the C_d and C_m values were multiplied by a correction factor of 2.2 and 0.8, respectively. This is consistent with prior investigation conducted in [33,65,66] that the coefficients C_d and C_m can vary due to the change in vibration amplitude and frequency. At this frequency, the displacement is notably smaller and this affects the signal-to-noise ratio in the data measured with the camera. This leads to a higher noise value in the beam-length/displacement plot, as shown in Fig. 13 (d) and (f). Despite the differences in the experimental and numerical results, the general trends can be observed.

4.3. Beam with $l = 13.5$ cm

The beam density was calculated from mass and volume measurements to be 7200 kg/m^3. The first five peaks from the FRF in Figure 10 (b) were used to estimate the flexural rigidity. Through numerical integration, the nonlinear coefficientsof the nonlinear damping model in Eq. (7) were determined: $\psi_{111} = 0.200$, $\psi_{222} = 0.175$, $\psi_{333} = 0.172$, $\psi_{444} = 0.157$, $\psi_{555} = 0.158$ and $\psi_{666} = 0.159$.

Fig. 14 presents a comparison between the numerical and experimental models generated using forcing frequencies near the second and third resonant frequencies. Fig. 14(a) reveals that the envelope of the analytical model does not reproduce the maximum amplitudes observed in the experimental measurements. As a remedy, a correction factor of 0.85 was applied to C_m in order to improve the envelope. Note that, in this case, applying the correction factor to C_m while leaving C_d unaltered is sufficient to improve the beam envelope as evident from the dotted black lines in Figure 14(a). At $f = 4$ Hz, the use of the correction factor was not necessary to approximate the envelope of the experimental model, as illustrated in Fig. 14(d). Furthermore, there is no significant discrepancy in the wave propagation patterns between the two models, particularly evident in the plot of maximum amplitudes with respect to t and x, shown in Fig. 14(c) and (f).

Fig. 15 shows a comparison between the nonlinear analytical and experimental models using forcing frequencies near the fourth and fifth resonant frequencies. The numerical model without the correction factor in C_d and C_m effectively approximates the experimental model even at higher modes. While a few nodal points in the analytical models might be slightly underestimated, as evident at the second trough of Fig. 15(a) and (d), no substantial disparities are noticeable. The envelope and the time series validation exhibit excellent agreement, highlighting the reliable performance of the mode shape and the modal coordinate in estimating the actual model.

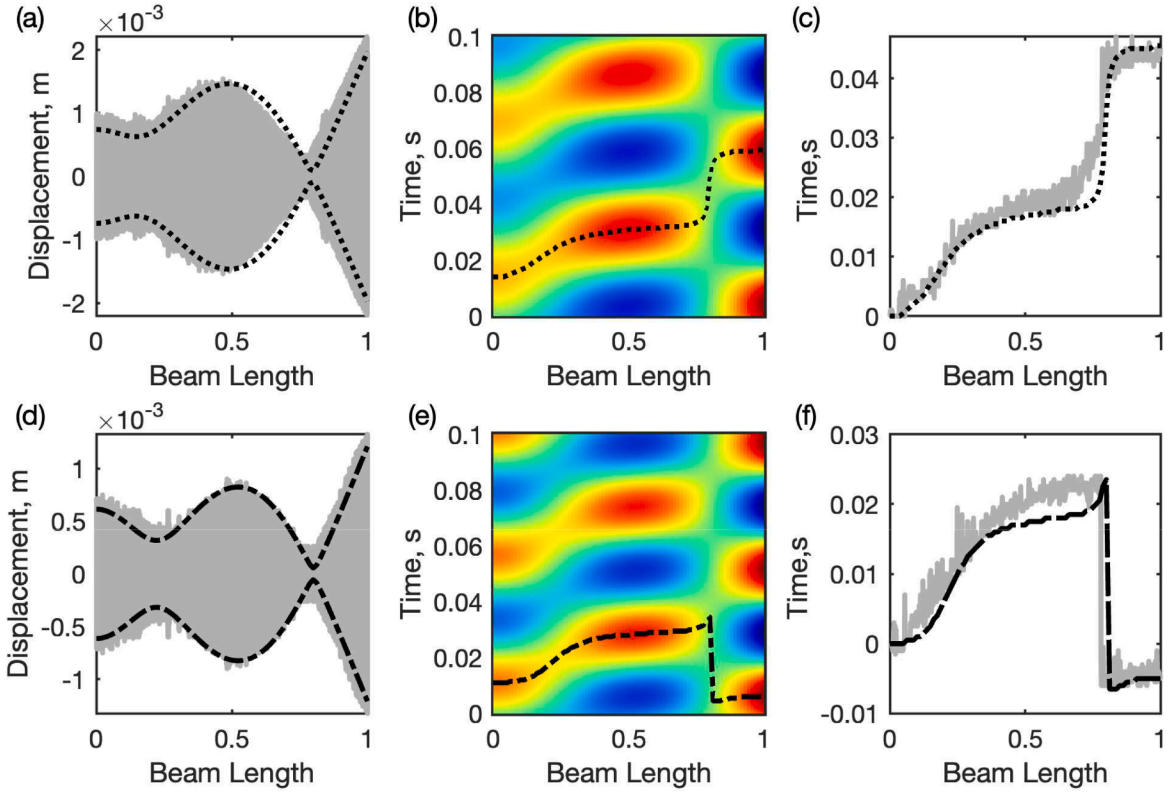

Fig. 13. Comparison of the analytical and experimental models. Panels (a), (b), and (c) were generated at 18 Hz and panels (d), (e), and (f) were actuated at 22 Hz. The grey lines indicate the experimental model. The dotted and dash-dotted black lines specify the numerical model with modified C_d and the numerical model with modified C_d and C_m, respectively. The envelope line and contour map in the second column refer to the analytical model. Panel (a) shows the displacement along the beam length, (b) depicts the time evolution of the beam's displacement, and (c) compares the time evolution between the experiment and simulation. Panels (d), (e), and (f) follow the same format for the higher frequency.

5. Discussion

This section addresses the implications of the findings from both the theoretical and experimental analyses. The discussion begins with examining the linear approximation, facilitating the connection between the dynamic behaviour of the beam's motion and mechanical wave phenomena. Following this, the analysis of passive travelling waves is presented, including a detailed description of the parameters contributing to their formation. This thorough analysis of the results enhances the understanding of passive travelling waves in beam-like structures and highlights potential directions for future research.

5.1. Linear approximation

It has been demonstrated that the analytical model with nonlinear damping can closely approximate the experimental measurements. The linear approximation model, however, is helpful in explaining the mechanical wave phenomena. The first row of Fig. 16 shows the comparison of the modal coordinates with respect to the frequency generated with the base amplitude, A_f, of 1.5 mm. The dotted blue lines represent q_i acquired through the application of the linear damping model as presented in Eq. (8). Conversely, the solid red lines depict the solution of q_i obtained from the quadratic damping model, as outlined in Eq. (A.6), considering solely the nonlinear coefficients $\psi_{111}\dot{q}_1|\dot{q}_1|$ and $\psi_{222}\dot{q}_2|\dot{q}_2|$ for the simulation.

It is evident that disparities arise near the natural frequencies, where the damping predicted by the linear model is underestimated in comparison to the nonlinear model. By eliminating the influence of the mode shape as outlined in Eq. (B.1), it is possible to explain why the linear and nonlinear models diverge near natural frequencies while converging at frequencies distant from resonance. As the forcing frequency approaches the natural frequency, the subtraction of $\omega_n^2 - \omega^2$ becomes close to zero. Consequently, the responses are primarily characterised by the cosine component of Eq. (B.1), which is directly proportional to the damping function, $2\zeta\omega_n\omega$. On the contrary, when the beam is actuated away from the natural frequencies, the sine component surpasses the cosine component, resulting in $\omega_n^2 - \omega^2 \gg 2\zeta\omega_n\omega$. Therefore, the damping holds minimal influence over the modal coordinates in such cases.

To address the issue of underestimated damping in the linear model, a correction factor $\chi(\omega)$ is introduced within the linear damping to more accurately estimate the nonlinear term $|\partial w/\partial t|\partial w/\partial t$. The dashed black lines in Fig. 16 demonstrate the responses of the linear model incorporating the correction factor. The variation of the correction factor across frequency is depicted separately and presented in the second row of Fig. 16. Ultimately, this facilitates the interpretation of wave phenomena on the beam through the insights developed in Section 2.2.

5.2. Passive travelling waves

For the case of the 8 cm beam, when the beam is actuated in the vicinity of the first resonance, the functions $U(\beta x)$ and $V(\beta x)$ have the same value due to the significant amount of damping. *Fig. 17* provides a schematic diagram illustrating the decomposition of the spatial function, including an illustrative example at $f = 2$ Hz. The magnitude of $U(\beta x)$ is essentially determined by $A_f + lp_1\varphi_1$, making $U(\beta x)$ non-zero at $x = 0$. Since $V(\beta x)$ gradually increases from zero and its temporal part is 90° out of phase with $U(\beta x)$, the sum of these spatial functions can form travelling waves. However, their magnitudes vary over the beam length and are not as uniform as in the example of full travelling waves illustrated in Fig. 2. This variation is due to the nature of the first mode shape

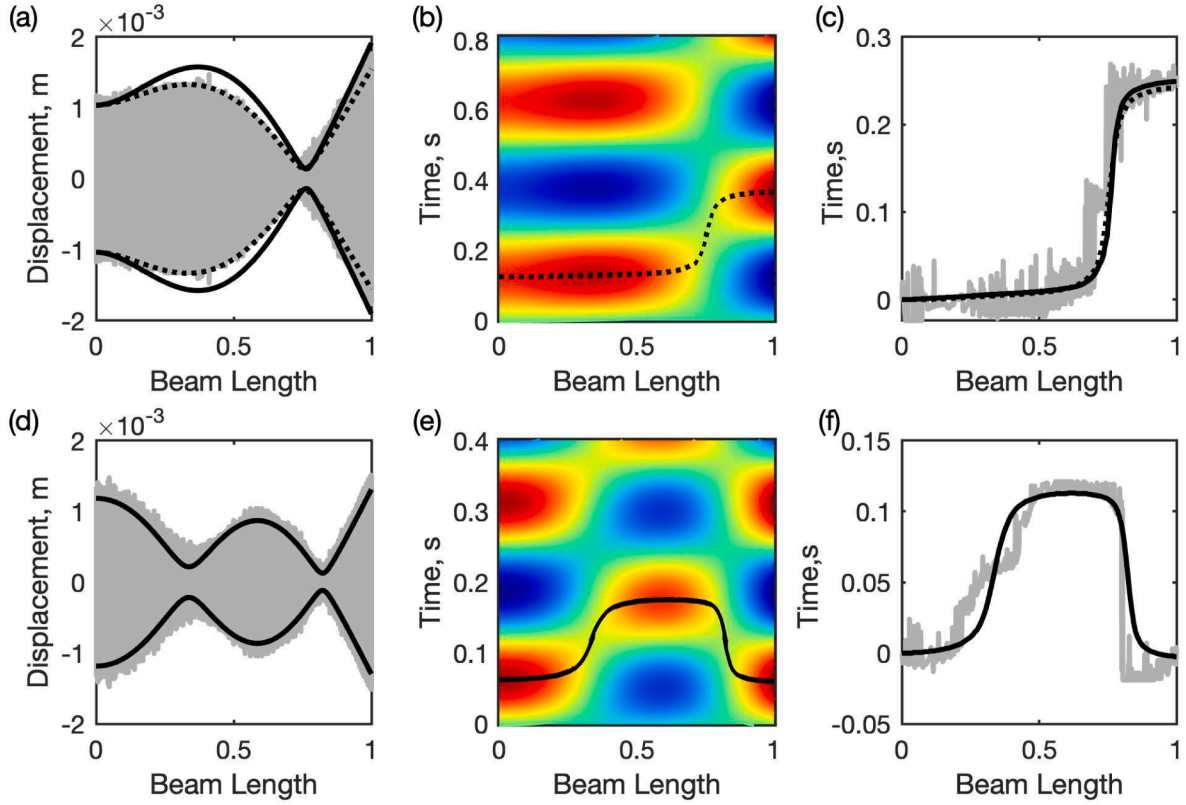

Fig. 14. Comparison of the analytical and experimental models. Panels (a), (b), and (c) were generated at 2 Hz and panels (d), (e), and (f) were actuated at 4 Hz. The grey lines indicate the experimental model. The solid and dotted black lines indicate the numerical model and numerical model with modified $\boldsymbol{C_m}$, respectively. The envelope line and contour map in the second column refer to the analytical model.

of the cantilever beam configuration.

Fig. 18(a) displays the upper view corresponding to the isometric representation shown in *Fig. 17*. The black line, representing max(w_t), is visualised separately from the contour plot in Fig. 18(b). It is clear that the slope is small. In theory, the slope of this line can be further increased by increasing the damping value to extend the magnitude of $V(\beta x)$ and, hence, increasing the phase delay between the beam tips. However, this is practically inconvenient. Changing the fluid characteristics, for example, will affect the Reynolds number which in turn alters not only the damping but also the added mass coefficients [36]. The existence of the travelling waves in this configuration occurs in a very limited frequency range. Beyond the first resonance, the function of $U(\beta x)$ transforms into $A_f - lp_1\varphi_1$ as a consequence of the term $(\omega_{n1}^2 - \omega^2)$. Consequently, $U(\beta x)$ exhibits negative values along the beam's length, as depicted in Figure 19(a). At the point of zero-crossing for $U(\beta x)$, a nodal point can emerge when a minor contribution from $V(\beta x)$ is considered. In Figure 18(b), the red line represents the peak amplitude of the beam with respect to t and x, observed at $f = 3$ Hz. A comparison between the black and red lines highlights the substantial impact that the sign (positive or negative) in the variable lp_1 can significantly transform the shape of the lines. As frequencies increase, such as at $f = 4$ Hz, the zero-crossing point undergoes a shift towards the right or towards the free end of the beam. This phenomenon is exemplified by the displacement of the blue line shown in Figure 18(b).

When the beam is forced close to the second mode, for instance at $f =$ 16 Hz, the constants lp_1, lp_2, rp_1 and rp_2 are all in the same order of magnitude. Consequently, the spatial functions are governed by equations containing the sum of the first two modes, leading to expressions $U(\beta x) = (A_f - lp_1\varphi_1 + lp_2\varphi_2)$ and $V(\beta x) = (rp_1\varphi_1 + rp_2\varphi_2)$. The graphical representation of these functions with respect to the beam length is depicted in Figure 19(a). The figure illustrates that the discontinuity observed in the travelling wave generated at this frequency arises from the proximity of the zero-crossing points between the two spatial functions. Additionally, it can be inferred that the observed inclination of the wave, denoted by the black line in Figure 19(b), is due to the significant contribution of $V(\beta x)$ which surpasses the effect of $U(\beta x)$. However, $V(\beta x)$ tends to deteriorate when the beam is forced away from resonance. Inevitably, this reduces the intensity of the travelling waves. These arguments are visually represented in Figure 19(c), which displays the evolution of the travelling contribution across various frequencies. As anticipated, the slope of the maximum beam amplitude curve experiences a steep decline as the beam's excitation is moved farther from the second resonance.

At $f = 18$ Hz (or beyond the second resonance) shown in Fig. 19, $U(\beta x)$ is described by the relation $(A_f - lp_1\varphi_1 - lp_2\varphi_2)$, featuring two zero-crossing points at approximately 0.3 L and 0.8 L. The magnitude of $V(\beta x)$ at 0.3 L, as depicted in Figure 19(d), can compensate for the nodal point formation in the beam envelope. This is why the beam the beam envelope at $f = 18$ Hz exhibits only one node. As the beam is actuated further away from resonance, for instance at an intermediate point between the second and third resonances depicted in Figure 13(d), $U(\beta x)$ predominates over the responses due to the subtraction of $\omega_{ni}^2 - \omega^2$. On the other hand, rp_1, rp_2 and rp_3 contribute less to the beam equation. Hence, the beam displacement given in Eq. (B.1) mainly comprises the sine part. Since the input base and relative beam motion are in phase, the total responses create hybrid waves containing fewer travelling waves.

For the case of the 13.5 cm beam, the slope of the travelling components around the second mode does not exhibit a more pronounced angle compared to the previous beam model. The transverse velocity of the beam in this mode is exceptionally low, and the squaring of the velocity term in the beam equation results in the damping function that approaches zero. As a result, the variable rp_i is comparatively lower than its counterpart, lp_i. Moreover, the first natural frequency's value drops

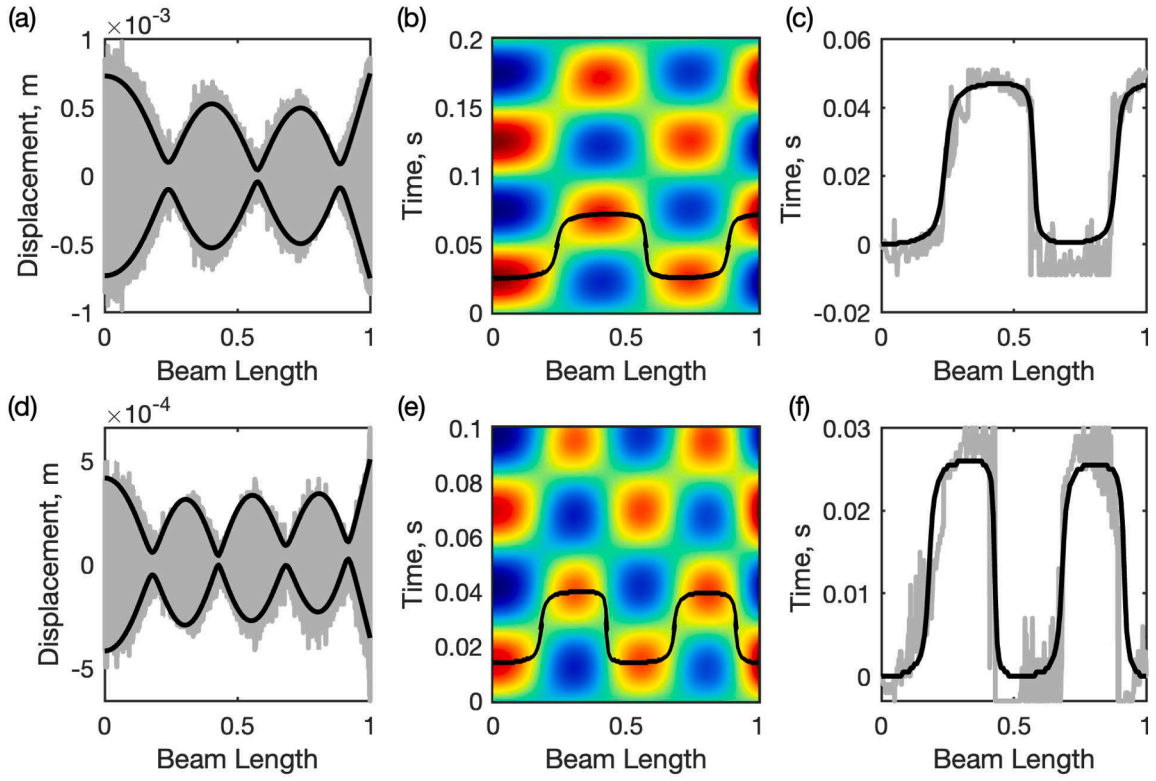

Fig. 15. Comparison of the analytical and experimental models. Panels (a), (b), and (c) were generated at 10 Hz and panels (d), (e), and (f) were actuated at 18 Hz. The grey and solid black lines signify the experimental model and the numerical model, respectively. The envelope line and contour map in the second column refer to the analytical model.

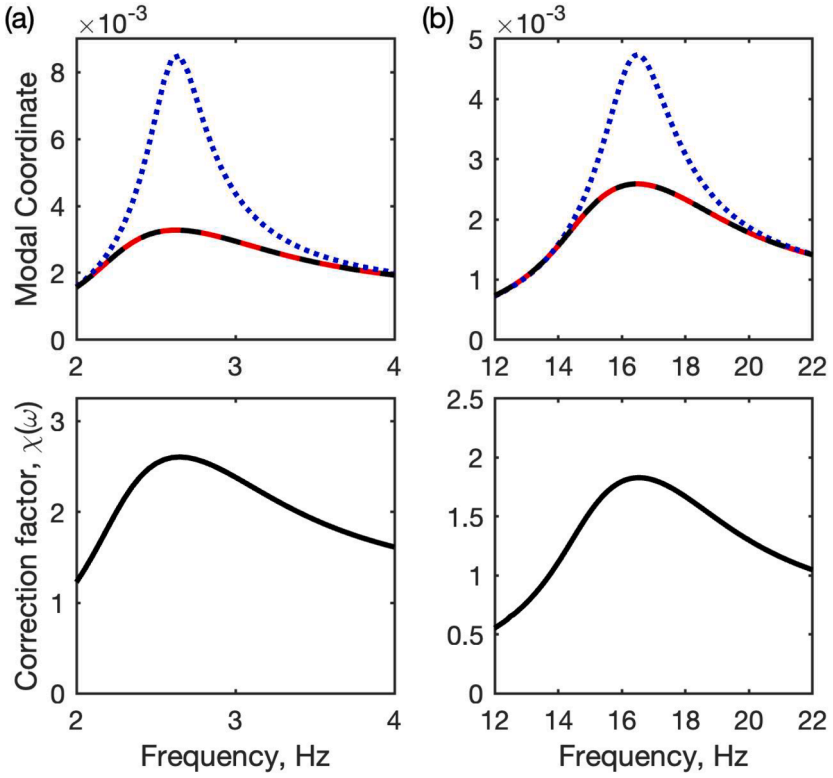

Fig. 16. Plot of the (a) first and (b) second modal coordinates with respect to frequency. In the modal coordinate plots, the solid red line represents the nonlinear model, the dotted blue line represents the linear approximation, and the dashed black line represents the linear approximation with the correction factor. The second row shows the correction factor corresponding to the plots in the first row.

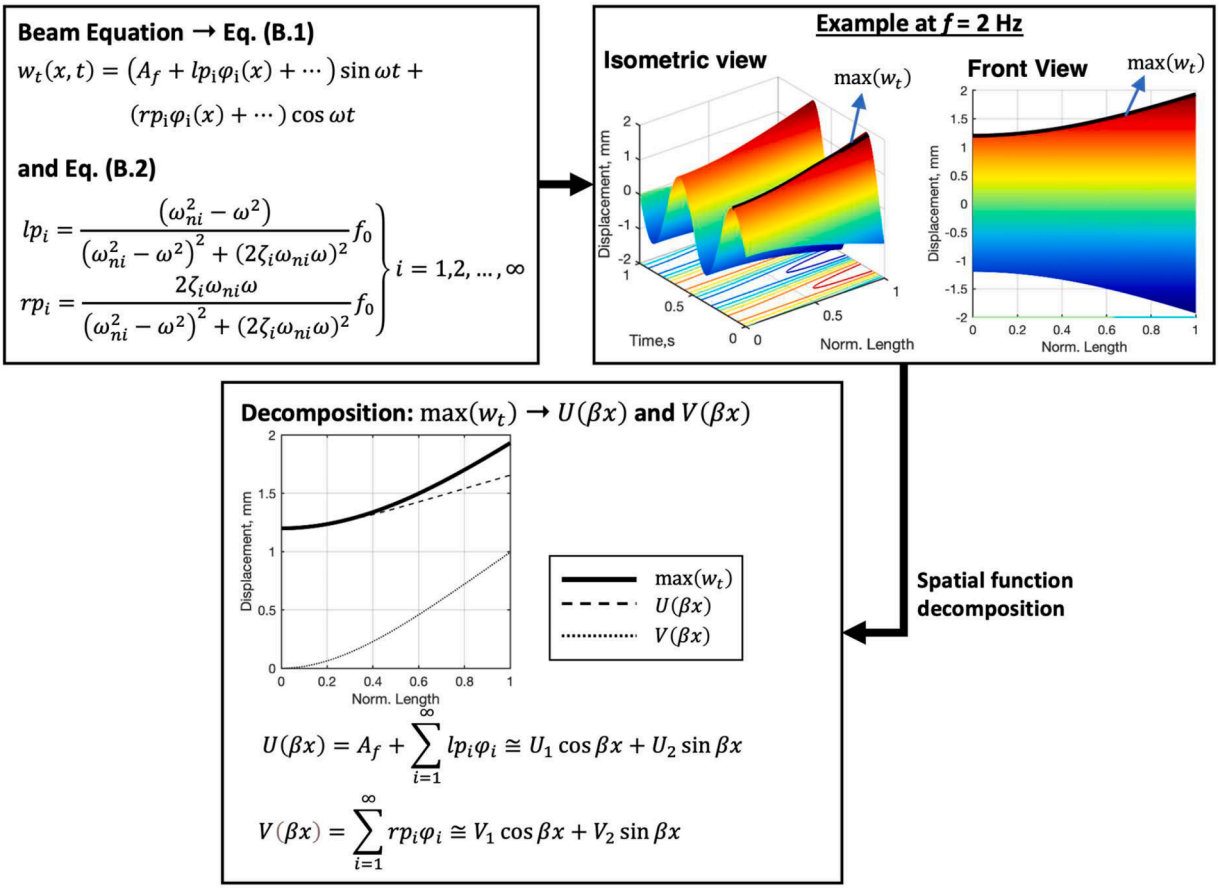

Fig. 17. Schematic diagram of spatial function decomposition. The beam equation is given by Eq. (B.1), which includes both sine and cosine terms with respective coefficients $\boldsymbol{l_{pi}}$ and $\boldsymbol{r_{pi}}$ as defined in Eq. (B.2). The isometric and front views show an example at $\boldsymbol{f = 2Hz}$, highlighting the maximum displacement max($\boldsymbol{w_t}$). The decomposition process is illustrated, where the maximum displacement max($\boldsymbol{w_t}$) is separated into spatial functions **U**($\boldsymbol{\beta x}$) and **V**($\boldsymbol{\beta x}$). The graph shows these components, with **U**($\boldsymbol{\beta x}$) and **V**($\boldsymbol{\beta x}$) represented by dashed and dotted lines, respectively.

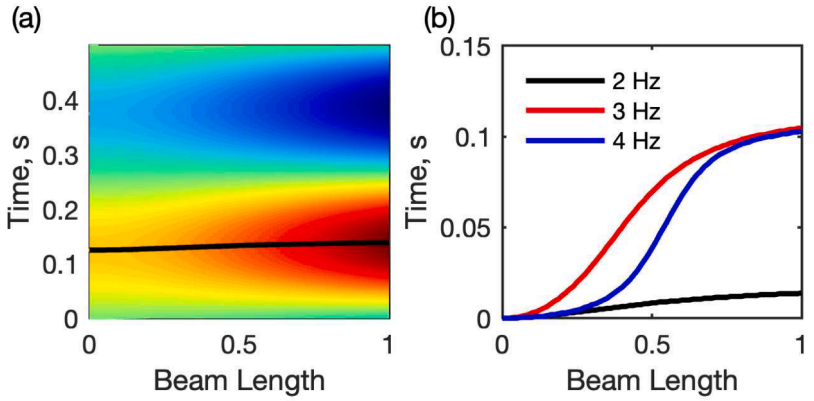

Fig. 18. (a) The contour map of the beam generated at 2 Hz and (b) the maximum amplitude of the beam against $\boldsymbol{t}$ and $\boldsymbol{x}$ for various frequencies. It compares the maximum amplitude of the beam for frequencies of 2 Hz (black), 3 Hz (red), and 4 Hz (blue). Note that an offset to $\boldsymbol{t} = 0$ was implemented for each individual frequency.

below 1 Hz, leading to a dominant proportion of lp_1 among the variables. As the forcing frequency is raised to $f = 4$ Hz, all parameters exhibit a similar order of magnitude, with the exception of rp_3. Consequently, the travelling waves become more prominent.

To further investigate the presence of a nodal point $x = 0.58$ L shown in Figure 15(a), the spatial functions of the beam generated at $f = 10$ Hz are plotted in Fig. 20(a). Evidently, the nodal point emerges as a consequence of the second zero-crossing point of $U(\beta x)$ which coincides with the trough of $V(\beta x)$. This pattern persists up to the fifth mode, where the nodal point occurs at $x = 0.43$ L as displayed in Figure 15(d). The plot of the spatial functions shown in Figure 20(b) illustrates that the nodal point is a result of the zero-crossing of $U(\beta x)$ intersecting with $V(\beta x)$. It is important to note that these nodal points at this particular length cannot be simply eliminated by increasing the damping. To address this issue, it is necessary to manipulate the spatial functions in a manner that causes the positions of the zero-crossing points between the

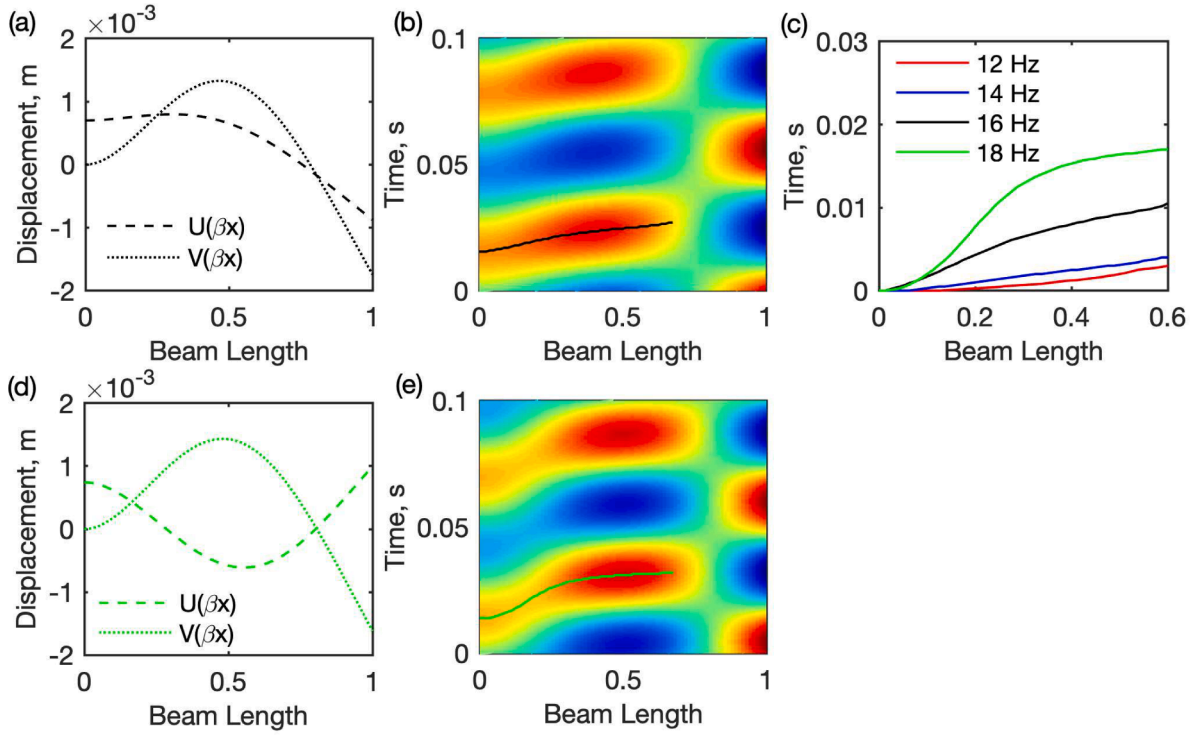

Fig. 19. (a) Plot of spatial functions and (b) location of the travelling part of the beam generated with 16 Hz. (c) The travelling parts of the 8 cm beam for various frequencies: 12 Hz (red), 14 Hz (blue), 16 Hz (black), and 18 Hz (green). (d) Spatial functions and (e) contour plot of the beam at 18 Hz.

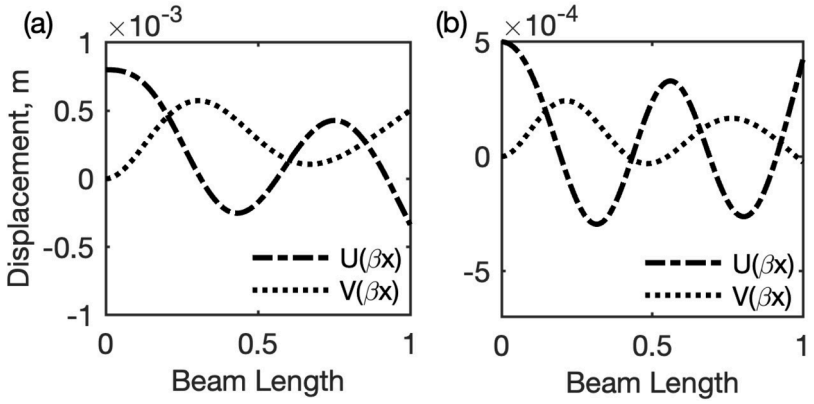

Fig. 20. The spatial function of the 13.5 cm beam at (a) $f = 10$ Hz and (b) $f = 18$ Hz, showing show the spatial functions $\mathbf{U}(\boldsymbol{\beta x})$ and $\mathbf{V}(\boldsymbol{\beta x})$, represented by the dash-dotted and dotted lines, respectively, along the beam length for the given frequencies.

two functions to shift, preventing their coincidental alignment. In practical terms, this objective can be attained through the application of two forces positioned around each end of the beam, while carefully regulating their associated forcing functions. This approach is often referred to as 'two-mode excitation' [14,15,50,67].

The characteristics of passive travelling waves are notably different from those of the two-mode excitation proposed by Loh and Ro [50]. Specifically, passive travelling waves occur at resonant frequencies, whereas travelling waves in the two-mode excitation system occur away from resonance. To illustrate this distinction, consider a beam vibrating at its first resonance, where $\omega = \omega_{n1}$. Under this condition, the total beam displacement is described by Equation (B.3), the mathematical derivation of which is detailed in Appendix B. Equation (B.3) closely resembles the model proposed by Loh and Ro [68], where a beam is excited by forces of identical frequency but with a 90-degree phase difference. However, a key difference lies in the constants $A_f\delta(x)$ in the sine term and $rp_1\varphi_1(x)$ in the cosine term, which results in less pure travelling waves compared to those described by Loh and Ro [68]. It is important to note that Loh and Ro's model assumes equal forcing values for both sine and cosine components.

In passive travelling waves, when the excitation frequency deviates from resonance (e.g., $\omega < \omega_{n1}$), the response of the beam can manifest as standing waves. This phenomenon is mathematically derived in Appendix B, as shown in Equation (B.4). This equation predicts the generation of standing waves, as the displacement of the beam is primarily a superposition of two sine functions. Equation (B.4) aligns with the two-mode excitation model shown in Eq. (B.5), particularly when it is excited at its natural frequencies.

6. Conclusions

This paper investigates the travelling waves of a slender beam

underwater with the aim of inducing propulsion. Analytical models based on linear and nonlinear damping have been developed, allowing the relationship between the beam displacement and the process that results in mechanical travelling waves to be investigated. In an initial examination of the beam in air, the backbone diagrams demonstrate that the beam possesses very weak nonlinearities which confirm the small displacement assumption made in the theoretical modelling. Further examination in the nonlinear damping model reveals that energy transfer between modes can be neglected, as demonstrated by the magnitude of cross-coupling coefficients in the model proposed. This assumption has been verified via a comparison between the analytical and experimental results for the case of a fully immersed beam, providing good agreement and therefore validating the assumption made.

It has been shown from experimental results that the highest amplitude travelling waves for a partially and fully submerged beam underwater are located in the neighbourhood of the natural frequencies. This is where the damping contributes the most to the beam equation, creating a phase delay in the propagation of the waves along the beam. The partially submerged beam model exhibits an interesting phenomenon around resonance in which the water absorbs the incoming wave to prevent its reflection and therefore the creation of standing waves. This results in intense travelling waves along the beam.

To expand the investigation into higher modes, a more flexible beam was also investigated. The underwater tests revealed that the beam possesses very dense natural frequencies as demonstrated by the number of peaks in the FRF up to 20 Hz. Particular attention has been given to the nodal points occurring at higher modes: these can affect the quality of the travelling waves creating a discontinuity in the wave and therefore affecting its suitability for propulsion. It has been demonstrated that the occurrences of the nodes are strongly dependent on the spatial functions that described the displacement of the beam. This has been thoroughly studied in the clamped-free beam configuration, but it can be generalised to other boundary conditions.

Finally, the use of the Galerkin method allowed us to investigate the relationship between the parameters contributing to the formation of travelling waves. This approach enabled us to understand how travelling waves are formed at resonant frequencies. Furthermore, this investigation expands the work done in [15,69] contributing to the development of efficient devices propelled via travelling waves. In particular, this work enables the implementation of a control strategy which requires a single point excitation and relegates the two-mode excitation only to those frequency ranges away from resonance where high-amplitude travelling waves are difficult to achieve. This comes with a considerable reduction in input power. This investigation complements the work on fluid-structure interaction presented by the authors in [19,70] where the effect of the travelling wave on the surrounding fluid is presented.

Since the forcing frequencies in this study are limited, future studies should consider higher frequencies and variations in input amplitude to explore the amplitude contributions of the modes adjacent to the forcing frequency, thereby determining the optimal actuation methods. Additionally, further research is needed to investigate how the boundary conditions change as the beam transitions from vibrating in air to being partially submerged and fully submerged, to better understand the phenomena.

CRediT authorship contribution statement

Skriptyan N.H. Syuhri: Conceptualization, Formal analysis, Investigation, Methodology, Software, Writing – original draft, Writing – review & editing, Visualization. **Hossein Zare-Behtash:** Writing – review & editing, Supervision, Resources, Project administration, Methodology, Investigation, Funding acquisition, Formal analysis, Conceptualization. **Andrea Cammarano:** Writing – review & editing, Supervision, Software, Resources, Project administration, Methodology, Investigation, Funding acquisition, Formal analysis, Conceptualization.

Declaration of competing interest

The authors declare that they have no known competing financial interests or personal relationships that could have appeared to influence the work reported in this paper.

Data availability

The authors do not have permission to share data.

Acknowledgements

S.N.H. Syuhri acknowledges the support of the Islamic Development Bank (IsDB).

Appendix A: Mathematical Derivations for Section 2.1

Substituting the method of separation variables given in Eq. (3) into an unforced Euler-Bernoulli beam equation results in:

$$\frac{a^2}{\varphi(x)}\frac{\partial^4\varphi(x)}{\partial x^4} = -\frac{1}{q(t)}\frac{\partial^2 q}{\partial t^2} = \omega^2, \tag{A.1}$$

where the term ω^2 has been introduced to represent the frequency equation that is associated with the temporal part and $a = EI/\mu$. Equation (A.1) consists of two equations: a second-order derivative with respect to t, and a fourth-order derivative with respect to x. Therefore, it requires two initial conditions and four boundary conditions to obtain the individual solution of the spatial and temporal functions. For the case of the clamped-free beam, the boundary conditions can be modelled by assuming zero deflection and slope at the clamped end, and zero bending moment and shear force at the free end. Enforcing these conditions leads to the formulation of the mode shape equation, $\varphi_i(x)$, in Eq. (4).

The mathematical derivation in Equation (A.1) is independent of damping and forcing functions, and is helpful to attain the mode shape of the beam. It is worth mentioning that there is no clear understanding on how to derive the mathematical model of damping mechanism in finite structures. Depending on the system being considered, the damping term can be integrated with the beam equation before or after applying the method of separation variables. In this study, the damping is applied to the beam equation by incorporating Eq. (5) into the Euler-Bernoulli beam equation. By applying the separation variables from Eq. (3) the following is obtained:

$$(\mu + M)\sum_{j=1}^{\infty}\varphi_j(x)\ddot{q}_j(t) + C_{ld}\sum_{j=1}^{\infty}\varphi_j(x)\dot{q}_j(t) + C_{qd}\sum_{j=1}^{\infty}\left|\varphi_j(x)\dot{q}_j(t)\right|\sum_{k=1}^{\infty}\varphi_k(x)\dot{q}_k(t) \quad + EI\sum_{j=1}^{\infty}\frac{\partial^4\varphi_j(x)}{\partial x^4}q_j(t) = F(x,t), \tag{A.2}$$

where C_{ld} is the linear damping due to the material, $M = 0.25\pi\rho_f C_m b^2$, $C_{qd} = 0.5\rho_f C_d b$ and $F(x,t) = -(\mu + M)\ddot{w}_b(x,t)$. Multiplying Eq. (A.2) with an

arbitrary mode shape, φ_i providing that $i \neq j$, and then integrating over the length of the beam, L, yields:

$$(\mu + M)\sum_{j=1}^{\infty}\int_0^L \varphi_j\varphi_i dx\ddot{q}_j + C_{ld}\sum_{j=1}^{\infty}\int_0^L \varphi_j\varphi_i dx\dot{q}_j + C_{qd}\sum_{j=1}^{\infty}\sum_{k=1}^{\infty}\int_0^L |\varphi_j|\varphi_k\varphi_i dx\dot{q}_k\left|\dot{q}_j\right| + EI\sum_{j=1}^{\infty}\int_0^L \frac{\partial^4\varphi_j}{\partial x^4}\varphi_i dx q_j = \int_0^L F(x,t)\varphi_i dx, \tag{A.3}$$

By using orthogonality conditions, Equation (A.3) can be expressed as an infinite series of independent equations of which the i-th mode is given by:

$$(\mu + M)\int_0^L \varphi_i\varphi_i dx\ddot{q}_i + C_{ld}\int_0^L \varphi_i\varphi_i dx\dot{q}_i + C_{qd}\sum_{j=1}^{\infty}\sum_{k=1}^{\infty}\int_0^L |\varphi_j|\varphi_k\varphi_i dx\dot{q}_k\left|\dot{q}_j\right| + EI\sum_{j=1}^{\infty}\int_0^L \frac{\partial^4\varphi_i}{\partial x^4}\varphi_i dx q_i = \int_0^L F(x,t)\varphi_i dx, \tag{A.4}$$

The definitions of mode-shapes, when $i = j$, satisfy:

$$\begin{cases} \int_0^L \varphi_i\varphi_i dx = L, \\ \int_0^L \varphi_i'''\varphi_i dx = \dfrac{\beta_i^4}{L^3}. \end{cases} \tag{A.5}$$

The terms $\psi_{jki}\ddot{q}_k(t)\left|\dot{q}_j(t)\right|$ in Eq. (6) can lead to multiple coefficients depending on the number of modes used in the simulation. To illustrate this, the first two modes, $i = 1, 2$, are used for the nonlinear modal coordinate equation which gives:

$$\begin{cases} \ddot{q}_1 + 2\zeta_{ld,1}\omega_{n1}\dot{q}_1 + \dfrac{C_{qd}}{(\mu+M)L}(\psi_{111}\dot{q}_1|\dot{q}_1| + \psi_{121}\dot{q}_1|\dot{q}_2| + \psi_{211}\dot{q}_2|\dot{q}_1| + \psi_{221}\dot{q}_2|\dot{q}_2|) + \omega_{n1}^2 q_1 = Q_1, \\ \ddot{q}_2 + 2\zeta_{ld,2}\omega_{n2}\dot{q}_2 + \dfrac{C_{qd}}{(\mu+M)L}(\psi_{112}\dot{q}_1|\dot{q}_1| + \psi_{122}\dot{q}_1|\dot{q}_2| + \psi_{212}\dot{q}_2|\dot{q}_1| + \psi_{222}\dot{q}_2|\dot{q}_2|) + \omega_{n2}^2 q_2 = Q_2. \end{cases} \tag{A.6}$$

Equation (A.6) contains a nonlinear damping term which requires numerical integration to obtain the solution of q_1 and q_2.

Appendix B: Mathematical Derivations for Section 2.2 and 5.2

The complete solution for the steady-state beam vibration, $w_t(x,t)$, can be realised by multiplying the modal coordinate, $q_i(t)$, with the mode shape, $\varphi_i(x)$, and considering the relative motion of the beam expressed in Eq. (1) to give:

$$\begin{aligned} w_t(x,t) \quad = \quad & A_f\delta(x)\sin\omega t + (lp_1\varphi_1(x) + lp_2\varphi_2(x) + \ldots)\sin\omega t \\ & + (rp_1\varphi_1(x) + rp_2\varphi_2(x) + \ldots)\cos\omega t, \end{aligned} \tag{B.1}$$

where the terms lp and rp are constants defined as

$$\left.\begin{aligned} lp_i &= \frac{(\omega_{ni}^2 - \omega^2)}{(\omega_{ni}^2 - \omega^2)^2 + (2\zeta_i\omega_{ni}\omega)^2} f_0 \\ rp_i &= \frac{2\zeta_i\omega_{ni}\omega}{(\omega_{ni}^2 - \omega^2)^2 + (2\zeta_i\omega_{ni}\omega)^2} f_0 \end{aligned}\right\} i = 1, 2, \ldots, \infty, \tag{B.2}$$

whereas $f_0 = \left(A_f\omega_f^2/L\right)\int_0^L \varphi_i(x)dx$.

Let us take an example of the beam vibrating at the first resonance, $\omega = \omega_{n1}$. Accordingly, the terms lp_1 in Eq. (B.1) becomes equal to zero due to numerator $(\omega_{n1}^2 - \omega^2) = 0$ in Eq. (B.2). In contrast, rp_1 becomes maximum due to denominator $2\zeta_1\omega_{n1}\omega/(2\zeta_1\omega_{n1}\omega)^2$. The other higher mode contributions, such as lp_2,lp_3,… and rp_2,rp_3,… are negligible. This condition leads to the total beam displacement of:

$$w_t(x,t) = A_f\delta(x)\sin\omega t + rp_1\varphi_1(x)\cos\omega t. \tag{B.3}$$

In case the beam vibrating away from resonance, for instance $\omega_{n1} > \omega$, the term rp_1will be close to zero, while the term lp_1 is at its maximum value. Neglecting the small contribution from the higher modes, the total beam equation becomes:

$$w_t(x,t) = A_f\delta(x)\sin\omega t + lp_1\varphi_1(x)\sin\omega t. \tag{B.4}$$

As a comparison, the two-mode excitation model proposed by Loh and Ro [68] is:

$$w_t(x,t) = P\cos\omega t\sum_{i=1}^{\infty}\frac{\varphi_i(x)\varphi_i(l_1)}{\omega_{ni}^2 - \omega^2} + P\sin\omega t\sum_{i=1}^{\infty}\frac{\varphi_i(x)\varphi_i(l_2)}{\omega_{ni}^2 - \omega^2}, \tag{B.5}$$

where P is the forcing magnitude, l_1 and l_2 are the location of the forcing function. Accordingly, if the two-mode excitation is forced in non-resonant conditions, for instance $\omega < \omega_{n1}$, Eq. (B.5) becomes identical to Eq. (B.3) except for the magnitude of travelling waves.

Appendix C: Data Acquisition for Partially Submerged Beam

Fig. E.1(a) shows a sample image of a partially submerged beam. Pixel acquisition was hindered by a displacement discontinuity caused by the change of refraction index at the air-water interface, as illustrated in Fig. E.1(b). Consequently, this interface region was eliminated, and the two sections were merged by offsetting the submerged part of the beam of a quantity equal to the gap at the interface. Subsequently, the amplitude was

normalised against the maximum displacement measured at the root of the beam.

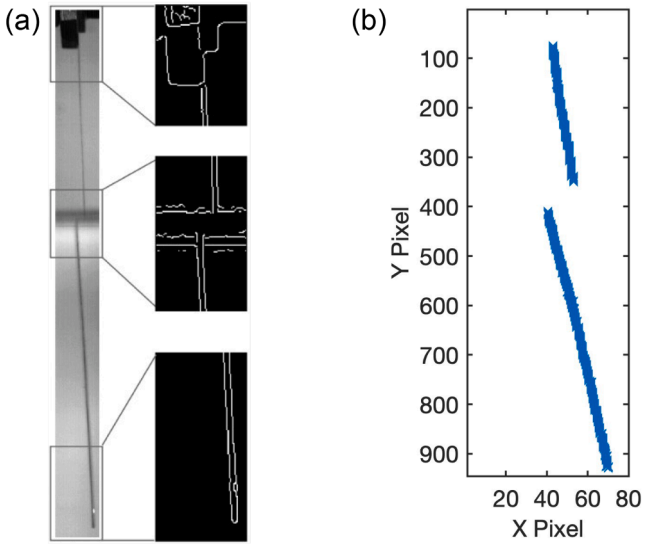

Fig. E.1. (a) A cropped image of the partially submerged beam, showing a detailed view of the beam and highlighting the conversion from a true colour image to a binary logical image in different sections. (b) Effect of the reflection on the pixel coordinates, illustrating how the reflection impacts the recorded pixel positions.

References

[1] Cen L, Erturk A. Bio-inspired aquatic robotics by untethered piezohydroelastic actuation. Bioinspir Biomim 2013;8(1).
[2] Erturk A, Delporte G. Underwater thrust and power generation using flexible piezoelectric composites: an experimental investigation toward self-powered swimmer-sensor platforms. Smart Mater Struct 2011;(12):20.
[3] Ramananarivo S, Godoy-Diana R, Thiria B. Passive elastic mechanism to mimic fish-muscle action in anguilliform swimming. J R Soc Interface 2013;10(88).
[4] Liu G, Zhang W. Travelling-Wave Micropumps. Microbial Toxins 2017:1–19.
[5] Ye W, et al. Travelling wave magnetic valveless micropump driven by rotating integrated magnetic arrays. Micro Nano Lett 2014;9(4):232–4.
[6] Zhang W, et al. Travelling-wave piezoelectric micropump with low resistance microchannel. Electron Lett 2011;47(19).
[7] Cui Z, Yang Z, Shen L, Jiang HZ. Complex modal analysis of the movements of swimming fish propelled by body and/or caudal fin. Wave Motion 2018;78:83–97.
[8] Zhang L, et al. Achieving travelling wave drag reduction by micro piezoelectric actuator. Int J Mech Sci 2024:275.
[9] Loh B-G, Ro PI. An object transport system using flexural ultrasonic progressive waves generated by two-mode excitation. IEEE Trans Ultrason Ferroelectric Frequency Control 2000;47(4):994–9.
[10] Bucher I. Estimating the ratio between travelling and standing vibration waves under non-stationary conditions. J Sound Vib 2004;270(1–2):341–59.
[11] Gabai, R. and I. Bucher, Generating traveling vibration waves in finite structures. 2008: p. 761–70.
[12] Hariri H, Bernard Y, Razek A. A two dimensions modeling of non-collocated piezoelectric patches bonded on thin structure. Curved Layered Struct 2014;2(1).
[13] Hariri H, Bernard Y, Razek A. Dual piezoelectric beam robot: the effect of piezoelectric patches' positions. J Intell Mater Syst Struct 2015;26(18):2577–90.
[14] Malladi VVNS. Continual traveling waves in finite structures: theory, simulations, and experiments. Blacksburg, Virginia: Virginia Polytechnic Institute and State University; 2016.
[15] Musgrave PF. Electro-hydro-elastic modeling of Structure-Borne Traveling Waves and their application to aquatic swimming motions. J Fluids Struct 2021:102.
[16] Musgrave PF, Sriram Malladi VVN, Tarazaga PA. Generation of Traveling Waves in a 2D Plate for Future Drag Reduction Manipulation. Special Topics in Structural Dynamics 2016;6:129–38.
[17] Musgrave PF, Albakri MI, Phoenix AA. Guidelines and procedure for tailoring high-performance, steady-state traveling waves for propulsion and solid-state motion. Smart Materials and Structures 2021;(2):30.
[18] Wang L, et al. A millipede-inspired miniature self-moving ultrasonic actuator with high carrying capability and nanometer resolution. Int J Mech Sci 2024:267.
[19] Syuhri SNH, Pickles D, Zare-Behtash H, Cammarano A. Influence of travelling waves on the fluid dynamics of a beam submerged in water. J Fluids Struct 2023:121.
[20] Kuribayashi M, Ueha S, Mori E. Excitation conditions of flexural traveling waves for a reversible ultrasonic linear motor. J Acoust Soc Am 1985;77(4):1431–5.
[21] Gabai R, Bucher I. Excitation and sensing of multiple vibrating traveling waves in one-dimensional structures. J Sound Vib 2009;319(1–2):406–25.
[22] Tanaka N, Kikushima Y. Active wave control of a flexible beam. proposition of the active sink method. JSME Int J Ser. 3, Vibrat Control Eng Eng Ind 1991;34(2):159–67.
[23] Ghenna S, et al. Modelling and control of a travelling wave in a finite beam, using multi-modal approach and vector control method. In: 2015 Joint Conference of the IEEE International Frequency Control Symposium & the European Frequency and Time Forum; 2015. p. 509–14.
[24] Gabay R, Bucher I. On Vibrating Traveling Waves Actuation. Sensing Tun Finite Struct 2006;2006:809–17.
[25] Blanchard A, et al. Mode complexity in a harmonically forced string with a local spring–damper and transitions from vibrations to waves. J Sound Vib 2015;334:282–95.
[26] Blanchard A, McFarland DM, Bergman LA, Vakakis AF. Damping-induced interplay between vibrations and waves in a forced non-dispersive elastic continuum with asymmetrically placed local attachments. In: Proceedings of the Royal Society A: Mathematical, Physical and Engineering Sciences. 471; 2015.
[27] Minikes A, Gabay R, Bucher I, Feldman M. On the sensing and tuning of progressive structural vibration waves. IEEE Trans Ultrason Ferroelectr Freq Control 2005;52(9):1565–76.
[28] Kumar A, DasGupta A. Generation of harmonic waves in beams using boundary excitation. Int J Mech Sci 2019;159:234–45.
[29] Ramananarivo S, Godoy-Diana R, Thiria B. Propagating waves in bounded elastic media: transition from standing waves to anguilliform kinematics. EPL (Europhysics Lett) 2014;(5):105.
[30] Ahsan SN. Modulation of hydrodynamic forces on oscillating submerged structures in viscous fluids. Reno: University of Nevada; 2018.
[31] Hu L, Yan H, Zhang W-M, Zou H-X, Peng Z-K, Meng G. Theoretical and experimental study on dynamic characteristics of V-shaped beams immersed in viscous fluids: From small to finite amplitude. J. Fluids Struct. 2018;82:215–44.
[32] Ahsan SN, Aureli M. Finite amplitude oscillations of flanged laminas in viscous flows: vortex–structure interactions for hydrodynamic damping control. J Fluids Struct 2015;59:297–315.
[33] Phan CN, Aureli M, Porfiri M. Finite amplitude vibrations of cantilevers of rectangular cross sections in viscous fluids. J Fluids Struct 2013;40:52–69.
[34] Phan CN, Porfiri M. Finite amplitude vibrations of square cross section beams in viscous fluids. Renewable energy systems; robotics; robust control; single track vehicle dynamics and control; stochastic models, control and algorithms in robotics, 3. Structure Dynamics and Smart Structures; 2012. p. 661–8.
[35] Intartaglia C, Soria L, Porfiri M. Hydrodynamic coupling of two sharp-edged beams vibrating in a viscous fluid. In: Proceedings of the Royal Society A: Mathematical, Physical and Engineering Sciences. 470; 2014.
[36] Xiu H, Davis RB, Romeo RC. Edge clearance effects on the added mass and damping of beams submerged in viscous fluids. J Fluids Struct 2018;83:194–217.
[37] Sader JE. Frequency response of cantilever beams immersed in viscous fluids with applications to the atomic force microscope. J Appl Phys 1998;84(1):64–76.
[38] Chon JWM, Mulvaney P, Sader JE. Experimental validation of theoretical models for the frequency response of atomic force microscope cantilever beams immersed in fluids. J Appl Phys 2000;87(8):3978–88.
[39] Green CP, Sader JE. Torsional frequency response of cantilever beams immersed in viscous fluids with applications to the atomic force microscope. J Appl Phys 2002;92(10):6262–74.
[40] Van Eysden CA, Sader JE. Frequency response of cantilever beams immersed in viscous fluids with applications to the atomic force microscope: arbitrary mode order. J Appl Phys 2007;101(4).

[41] Van Eysden CA, Sader JE. Frequency response of cantilever beams immersed in compressible fluids with applications to the atomic force microscope. J Appl Phys 2009;(9):106.
[42] Green CP, Sader JE. Frequency response of cantilever beams immersed in viscous fluids near a solid surface with applications to the atomic force microscope. J Appl Phys 2005;(11):98.
[43] Green CP, Sader JE. Small amplitude oscillations of a thin beam immersed in a viscous fluid near a solid surface. Phys Fluids 2005;(7):17.
[44] Feeny BF. A complex orthogonal decomposition for wave motion analysis. J Sound Vib 2008;310(1–2):77–90.
[45] Feeny BF, Feeny AK. Complex modal analysis of the swimming motion of a whiting. J Vib Acoust 2013;(2):135.
[46] Bucher I, et al. Experimental travelling waves identification in mechanical structures. Math Mech Solids 2017;24(1):152–67.
[47] Erturk A, Inman DJ. An experimentally validated bimorph cantilever model for piezoelectric energy harvesting from base excitations. Smart Mater Struct 2009;18 (2).
[48] Erturk A, Inman DJ. On mechanical modeling of cantilevered piezoelectric vibration energy harvesters. J Intell Mater Syst Struct 2008;19(11):1311–25.
[49] Morison JR, Johnson JW, Schaaf SA. The force exerted by surface waves on piles. J Petrol Technol 1950;2(05):149–54.
[50] Byoung-Gook L, Ro PI. An object transport system using flexural ultrasonic progressive waves generated by two-mode excitation. IEEE Trans Ultrason Ferroelectric Frequen Control 2000;47(4):994–9.
[51] Syuhri SNH, McCartney A, Cammarano A. Development of an experimental rig for emulating undulatory locomotion. Nonlinear Struct Syst 2021;1:253–63.
[52] Londoño JM, Neild SA, Cooper JE. Identification of backbone curves of nonlinear systems from resonance decay responses. J Sound Vib 2015;348:224–38.
[53] Naylor S, Platten MF, Wright JR, Cooper JE. Identification of Multi-Degree of Freedom Systems With Nonproportional Damping Using the Resonant Decay Method. J Vib Acoust 2004;126(2):298–306.
[54] Abassi W, El Baroudi A, Razafimahery F. Vibration Analysis of Euler-Bernoulli Beams Partially Immersed in a Viscous Fluid. Physics Research International 2016; 2016:1–14.
[55] Ergin A, Uğurlu B. Linear vibration analysis of cantilever plates partially submerged in fluid. J Fluids Struct 2003;17(7):927–39.
[56] Hossain A, Humphrey L, Mian A. Prediction of the dynamic response of a mini-cantilever beam partially submerged in viscous media using finite element method. Finite Element Anal Des 2012;48(1):1339–45.
[57] Hossain A, Mishty A, Mian A. Numerical analysis for design optimization of microcantilever beams for measuring rheological properties of viscous fluid. Finite Element Anal Des 2013;68:1–9.
[58] Kwak MK, Yang D-H. Free vibration analysis of cantilever plate partially submerged into a fluid. J Fluids Struct 2013;40:25–41.
[59] Ma C, et al. Fluid structure interaction analysis of flexible beams vibrating in a time-varying fluid domain. In: Proceedings of the Institution of Mechanical Engineers, Part C: Journal of Mechanical Engineering Science. 234; 2020. p. 1913–27.
[60] Riesch C, Reichel EK, Keplinger F, Jakoby B. Characterizing vibrating cantilevers for liquid viscosity and density sensing. J Sens 2008;2008:1–9.
[61] Shao M, et al. Effects of time-varying fluid on dynamical characteristics of cantilever beams: numerical simulations and experimental measurements. Math Probl Eng 2020;2020:1–18.
[62] Vu VH, Thomas M, Lakis AA, Marcouiller L. Effect of added mass on submerged vibrated plates. Canadian machinery vibration association (CMVA 7). 2007.
[63] Koushesh A. Added mass formulation for fluid-structure interaction. United Arab Emirates: American University of Sarjah; 2016.
[64] Syuhri SNH, Zare-Behtash H, Cammarano A. Investigating the influence of fluid-structure interactions on nonlinear system identification. Vibration 2020;3(4): 521–44.
[65] Aureli M, Basaran ME, Porfiri M. Nonlinear finite amplitude vibrations of sharp-edged beams in viscous fluids. J Sound Vib 2012;331(7):1624–54.
[66] Aureli M, Porfiri M. Low frequency and large amplitude oscillations of cantilevers in viscous fluids. Appl Phys Lett 2010;96(16).
[67] Avirovik D, Malladi VVNS, Priya S, Tarazaga PA. Theoretical and experimental correlation of mechanical wave formation on beams. J Intell Mater Syst Struct 2016;27(14):1939–48.
[68] Loh BG, Ro PI. Changing the propagation direction of flexural ultrasonic progressive waves by modulating excitation frequency. J Sound Vib 2000;238(1): 171–8.
[69] Malladi VVNS, Albakri M, Musgrave P, Tarazaga PA. Investigation of propulsive characteristics due to traveling waves in continuous finite media. Bioinspiration, biomimetics, and bioreplication 2017. 2017.
[70] Syuhri S, Zare-Behtash H, Cammarano A. Experimental characterization of structural traveling wave-induced thrust. Special topics in structural dynamics & experimental techniques, 5; 2024. p. 27–35.